MNRAS 000, 1–22 (2026) Preprint 20 August 2026 Compiled using MNRAS LATEX style file v3.3

Quasar Impostors: Two Extremely UV-Bright ($M_{\rm UV} \approx -23.5$) Reionisation-Epoch Galaxies Powered by Very Massive Stars

Daming Yang (羊达明),[1★] Joseph F. Hennawi,[1,2] Sarah E. I. Bosman,[3,4] Frederick B. Davies,[4] Rychard Bouwens,[1] Timo Kist,[1] Eduardo Bañados,[4] Jiamu Huang,[2] Alice E. Shapley,[5] Marianne Vestergaard,[6,7] Hiddo S. B. Algera,[8] Silvia Belladitta,[4] Anna-Christina Eilers,[9,10] Xiaohui Fan,[7] Francesco Guarneri,[11] Xiangyu Jin,[12] Romain A. Meyer,[13] Elia Pizzati,[1,14†] Huub Röttgering,[1] Jan-Torge Schindler,[11] Mauro Stefanon,[15,16] Feige Wang[12] and Jinyi Yang[12]

[1]*Leiden Observatory, Leiden University, P.O. Box 9513, 2300 RA Leiden, The Netherlands*
[2]*Department of Physics, University of California, Santa Barbara, CA 93106, USA*
[3]*Institute for Theoretical Physics, Heidelberg University, Philosophenweg 12, D–69120, Heidelberg, Germany*
[4]*Max-Planck-Institut für Astronomie, Königstuhl 17, 69117 Heidelberg, Germany*
[5]*Department of Physics and Astronomy, University of California, Los Angeles, 430 Portola Plaza, Los Angeles, CA 90095, USA*
[6]*DARK, The Niels Bohr Institute, University of Copenhagen, Jagtvej 155, DK-2200 Copenhagen N, Denmark*
[7]*Steward Observatory, University of Arizona, 933 North Cherry Avenue, Tucson, AZ 85718, USA*
[8]*Institute of Astronomy and Astrophysics, Academia Sinica, 11F of Astronomy-Mathematics Building, No. 1, Sec. 4, Roosevelt Rd, Taipei 106319, Taiwan, R.O.C.*
[9]*MIT Kavli Institute for Astrophysics and Space Research, 77 Massachusetts Avenue, Cambridge, MA 02139, USA*
[10]*Department of Physics, Massachusetts Institute of Technology, 77 Massachusetts Avenue, Cambridge, MA 02139, USA*
[11]*Hamburg Observatory, University of Hamburg, Gojenbergsweg 112, D-21029 Hamburg, Germany*
[12]*Department of Astronomy, University of Michigan, 1085 South University Avenue, Ann Arbor, MI 48109, USA*
[13]*Department of Astronomy, University of Geneva, Chemin Pegasi 51, 1290 Versoix, Switzerland*
[14]*Center for Astrophysics | Harvard & Smithsonian, Cambridge, MA 02138, USA*
[15]*Departament d'Astronomia i Astrofísica, Universitat de València, C. Dr. Moliner 50, E-46100 Burjassot, València, Spain*
[16]*Unidad Asociada CSIC "Grupo de Astrofísica Extragaláctica y Cosmología" (Instituto de Física de Cantabria – Universitat de València), Spain*

Accepted XXX. Received YYY; in original form ZZZ

ABSTRACT

The extreme bright end of the galaxy UV luminosity function during reionisation remains poorly constrained, particularly where the galaxy and quasar luminosity functions overlap and source classification becomes ambiguous. We present *JWST*/NIRSpec and ALMA Band-6 observations of J1450−0144 ($z = 6.627$) and J1429−0104 ($z = 6.796$), two $M_{\rm UV} \simeq -23.5$ sources originally classified as faint quasars by SHELLQs. NIRSpec reveals blue UV continua, strong P Cygni profiles in N v, Si iv, and C iv, broad He ii λ1640 emission with rest-frame equivalent widths of 8.8 ± 1.2 and 3.7 ± 1.1 Å, respectively, and narrow nebular lines, reclassifying both as extremely UV-luminous galaxies. Standard population-synthesis models cannot simultaneously reproduce the strong He ii and wind features, whereas models incorporating very massive stars (VMS; $M \gtrsim 100\,M_\odot$) with dedicated wind prescriptions can. These models favor a star-formation duration of 2–4 Myr for J1450−0144, with a broader allowed range for J1429−0104, stellar masses of $\log(M_\star/M_\odot) \approx 9.2$–$9.9$, and star-formation rates of $\simeq 300$–$540\,M_\odot\,{\rm yr}^{-1}$. Under the same VMS wind models, equivalent-width diagnostics imply $M_{\rm up} \gtrsim 225\,M_\odot$ for J1429−0104, while J1450−0144 lies beyond even the $M_{\rm up} = 475\,M_\odot$ grid. ALMA detects luminous [C ii] 158 μm emission in both systems, with $L_{\rm [CII]} \approx 0.8$ and $4.1 \times 10^9\,L_\odot$, respectively. J1429−0104 additionally shows bright dust continuum, with both [C ii] and dust offset by ~ 5.4 kpc from its UV emission. These sources demonstrate that VMS can power some of the most UV-luminous galaxies at cosmic dawn and show that source classifications, and hence the inferred demographics of both galaxies and quasars in the crossover regime, need revisiting.

Key words: stars: massive – galaxies: high-redshift – galaxies: luminosity function, mass function – quasars: general – galaxies: starburst – dark ages, reionization, first stars

1 INTRODUCTION

The bright end of the galaxy UV luminosity function (UVLF) during the epoch of reionisation ($z \gtrsim 6$) remains poorly constrained. At $z \sim 7$, the bright end of the UVLF in Harikane et al. (2025) is constrained by only four galaxies with $M_{\rm UV} < -23$, and in

★ E-mail: dyang@strw.leidenuniv.nl
† NHFP Einstein Fellow

their brightest bin, $-24.5 < M_{\rm UV} < -23.5$, the number density is only a lower limit, based on a single galaxy. With so few sources contributing, the two LF forms considered in Harikane et al. (2025) give rather different number densities in these luminosity regimes: at $M_{\rm UV} = -23$ the double power-law (DPL) gives 154 $\rm Gpc^{-3}\,mag^{-1}$ against 40 $\rm Gpc^{-3}\,mag^{-1}$ for the Schechter function, and at $M_{\rm UV} = -24$, the extrapolation of the two diverge by four orders of magnitude, with the DPL giving $\sim 5\,\rm Gpc^{-3}\,mag^{-1}$ and the Schechter function $\sim 4\times10^{-4}\,\rm Gpc^{-3}\,mag^{-1}$. Even finding a modest sample of ten sources at $-24.5 < M_{\rm UV} < -23.5$ would require surveying $\sim 160\,\rm deg^2$ if the bright end follows the DPL, or close to the entire sky if it follows the Schechter function, far beyond the pencil-beam fields of *JWST* deep imaging programmes. However, the galaxies that do reach this regime are among the most extreme actively star-forming systems known at any epoch, with rest-frame UV luminosities ($\nu L_\nu \gtrsim 10^{45}\,\rm erg\,s^{-1}$ at 1500 Å) corresponding to star-formation rates of $\sim$ 100–1000 $\rm M_\odot\,yr^{-1}$. Whether such rates can be accommodated by standard star-formation prescriptions, or whether they instead require new ingredients, is unresolved. Proposed routes to sustain such intense UV emission include an elevated baryon-to-star conversion efficiency, in which a larger fraction of a halo's baryons are converted into stars (Dekel et al. 2023; Li et al. 2024); a non-standard IMF, either top-heavy or hosting substantial populations of very massive stars, raising the UV output per unit stellar mass formed (Trinca et al. 2024; Cueto et al. 2024; Schaerer et al. 2025), stochastic, bursty star-formation histories, under which these galaxies are captured at the peak of their UV fluctuations (Mason et al. 2023; Sun et al. 2023; Pallottini & Ferrara 2023; Shen et al. 2023), and radiation-driven outflows that decouple dust from the UV-emitting stars and reduce attenuation (Ferrara et al. 2023; Ziparo et al. 2023; Ferrara et al. 2025). Many of these mechanisms have also been invoked to explain the unexpected abundance of UV-luminous galaxies at $z > 10$ uncovered by *JWST* (e.g., Naidu et al. 2022; Castellano et al. 2022; Harikane et al. 2023; Finkelstein et al. 2023; Robertson et al. 2024). Those galaxies are fainter ($M_{\rm UV} \approx -19$ to -22) than the $M_{1450} \lesssim -23$ regime considered here, and at those redshifts individual sources rarely yield the spectroscopic and far-infrared signal-to-noise ratio needed to discriminate between the proposed mechanisms. Sources at the bright end of the reionisation-epoch UVLF are therefore the natural testbeds for these theories, where detailed multi-wavelength follow-up of individual systems becomes feasible.

Observational constraints on these mechanisms have so far been limited due to the small existing spectroscopic sample of bright galaxies during cosmic dawn. Identifying galaxies at $M_{1450} \lesssim -23$ at $z > 6$ in meaningful numbers requires hundreds to thousands of square degrees of imaging, accessible only to wide-area ground-based or space-based surveys. ALMA programmes such as REBELS (Bouwens et al. 2022) have followed up UV-bright candidates at $z \sim 7$ across $\sim 7\,\rm deg^2$ of the COSMOS, UDS, and XMM-LSS fields, yielding detailed [C II] 158 μm and dust-continuum constraints, but reach only $M_{\rm UV} \approx -22.9$ at their brightest and do not extend to $M_{1450} \lesssim -23$. Harikane et al. (2025) recently compiled a broader sample of spectroscopically confirmed bright galaxies at $z \sim$ 7–14 drawn from a wide range of programmes, covering $\gtrsim 100\,\rm deg^2$ in total. While they showed that the bright end of the $z \sim 7$ UV luminosity function is in excess of a Schechter extrapolation and better described by a DPL, the compilation contains only a handful of sources at $M_{1450} \lesssim -23$ and $z > 6$: HSC J023536−031737 ($z = 6.913$, $M_{\rm UV} = -23.6$; Ono et al. 2018; Harikane et al. 2022), UVISTA-304416 ($z = 7.060$, $M_{\rm UV} = -23.1$; Bowler et al. 2017; Schouws et al. 2023), HSC J084916+005311 ($z = 6.606$, $M_{\rm UV} = -23.1$; Harikane et al. 2022, 2025), and HSC J091519−012630 ($z = 7.0$, $M_{\rm UV} = -23.9$; Harikane et al. 2022, 2025). Several of these sources, however, still lack rest-frame UV spectroscopy of sufficient depth and wavelength coverage to characterise their stellar population, leaving both the AGN contamination and the physical drivers of the UV output open questions.

At the same time, the Subaru High-z Exploration of Low-Luminosity Quasars survey (SHELLQs; Matsuoka et al. 2016, 2018a,b, 2019, 2022, 2025) has also yielded a substantial sample of UV-bright galaxy candidates with $-22 > M_{1450} > -25$ at $z \sim 6$ during their quasar searches. Marques-Chaves et al. (2025) further stacked a subset of these galaxies with strong but narrow Lyα lines and showed that these sources are consistent with very young ($\sim$ 6 Myr) starbursts. However, the luminosity regime of $M_{1450} \approx -23$ to -25 is exactly where the faint end of the quasar luminosity function and the extreme bright end of the galaxy UVLF intersect, and a blue UV continuum paired with a prominent, moderately broad Lyα line is consistent with either a faint type-I quasar or an intensely star-forming galaxy. Distinguishing the two populations on the basis of discovery spectroscopy with low sensitivity alone is inherently ambiguous (e.g., Matsuoka et al. 2018a; Harikane et al. 2025). As a result, some fraction of sources classified as faint quasars may in fact be galaxies, and vice versa, with direct consequences for both the faint-end slope of the quasar luminosity function and the bright-end slope of the galaxy luminosity function.

Despite the observational difficulties at $z > 6$, similarly bright galaxies at $z \sim$ 2–4 have been uncovered and studied in detail, dubbed the Extreme UV Luminous Galaxies (EUVLGs; Marques-Chaves et al. 2020, 2021, 2022; Upadhyaya et al. 2024; Dessauges-Zavadsky et al. 2025). These galaxies have $M_{\rm UV}$ between −23 and −24.5 and SFRs of several hundred $\rm M_\odot\,yr^{-1}$. Their rest-frame UV spectra display blue continua, prominent P Cygni profiles in the high-ionisation wind lines N V λ1240, Si IV λ1400, and C IV λ1550, and narrow nebular emission consistent with H II-region rather than AGN excitation. SED modelling returns stellar ages of $\lesssim$ 10 Myr and specific star-formation rates of $\sim 100\,\rm Gyr^{-1}$, identifying EUVLGs as short-lived but extreme starburst phases. Cosmic-noon EUVLGs thus provide a template for what a bright, AGN-free star-forming galaxy looks like in this regime.

One of the most striking findings from these EUVLGs is the frequent detection of strong, broad He II λ1640 emission, with $\rm EW_0 \simeq$ 1.4–4.6 Å (Upadhyaya et al. 2024). Conventional population-synthesis models with IMF upper-mass cutoffs of $\sim 100\,\rm M_\odot$ cannot reproduce these signatures, which are instead characteristic of the dense, radiatively driven winds of very massive stars (VMS; $M \gtrsim 100\,\rm M_\odot$; see Vink et al. 2015, for a review). Comparable broad and strong He II features are seen most directly in the R136 cluster in the Large Magellanic Cloud, where individual VMS have been resolved and identified (Crowther et al. 2010, 2016), and in other local VMS-dominated star clusters or star-forming regions, such as Mrk 71-A, II Zw 40-A, and SB 126 (Leitherer et al. 2018; Senchyna et al. 2021; Smith et al. 2023; Martins et al. 2023). Most recently, Marques-Chaves et al. (2026) reported direct evidence for VMS in the reionisation epoch using data from the JWST program SPectroscopic Ultra-deep Reionisation-era Survey (SPURS, GO 9214; PIs: C. Mason & D. Stark). They reported broad He II emission and N V/C IV P Cygni profiles in two $z \simeq 8.7$ galaxies, CEERS-1019 ($M_{\rm UV} = -22.4$, He II EW = 4.53 ± 0.36 Å) and CEERS-1025 ($M_{\rm UV} = -21.2$, He II EW = 4.09 ± 0.71 Å), that are reproduced only by models including VMS. From the same programme, ultra-deep spectroscopy of GN-z11 ($M_{\rm UV} = -21.6$, $z = 10.6$) has revealed P Cygni wind features and broad He II emission that are jointly reproduced by models incorporating VMS at low metallicity and young ages ($\lesssim$ 3 Myr), extending the evidence for VMS to $z > 10$ (Chen et al. 2026). These discoveries have hinted at a potential link between extreme UV-brightness and the presence of VMS and/or atypical IMF emergence.

In this work, we address these questions using two exceptionally UV-luminous sources in the epoch of reionisation. We present *JWST*/NIRSpec and ALMA Band-6 observations of J1450−0144 ($z = 6.627$) and J1429−0104 ($z = 6.796$), originally classified as faint quasars by the SHELLQs survey (Matsuoka et al. 2018a, 2022). The new NIRSpec spectra show that both objects are better interpreted as extreme UV-luminous galaxies, rather than unobscured quasars, with rest-frame UV emission dominated by very young, intensely star-forming stellar populations. With $M_{1450} \approx -23.5$, these sources lie among the UV-brightest spectroscopically confirmed objects known at $z \gtrsim 6.5$. We use the combination of rest-UV spectroscopy, ALMA [C II] 158 μm observations, and dust-continuum constraints to investigate the physical nature of these sources and their implications for the abundance of EUVLGs at $z \sim 7$.

The paper is organised as follows. Sect. 2 describes the discovery of J1450−0144 and J1429−0104 and the follow-up JWST/NIRSpec and ALMA observations. In Sect. 3 we establish the EUVLG nature of both sources, model their stellar populations which could contain a substantial fraction of very massive stars, present the ALMA gas and dust measurements, and derive a lower limit on the EUVLG number density at $z \sim 7$. Sect. 4 discusses the combined UV–FIR view of the two systems and the implications of their VMS content, and we summarise our findings in Sect. 5. Throughout this work we adopt a flat ΛCDM cosmology with $H_0 = 70\,\mathrm{km\,s^{-1}\,Mpc^{-1}}$, $\Omega_\mathrm{m} = 0.3$, and $\Omega_\Lambda = 0.7$. All magnitudes are given in the AB system.

2 DISCOVERY AND FOLLOW-UP OBSERVATIONS OF J1429−0104 & J1450−0144

2.1 Initial discovery

J1429−0104 and J1450−0144 were first discovered in the Subaru High-z Exploration of Low-Luminosity Quasars (SHELLQs; e.g., Matsuoka et al. 2016) program. J1429−0104 was identified as a quasar at $z = 6.8$ using the Optical System for Imaging and low-Intermediate-Resolution Integrated Spectroscopy (OSIRIS; Cepa et al. 2000) on the Gran Telescopio Canarias (GTC). Its UV magnitude was estimated to be $M_{1450} \approx -23$, and its Lyα line was measured to have FWHM = 1400 ± 100 km s^{-1} and $L_{\mathrm{Ly}\alpha} \approx 10^{43.95}$ erg s^{-1} (Matsuoka et al. 2018a). J1450−0144 was identified as a quasar at $z = 6.63$ with $M_{1450} \approx -23.73$ using the Faint Object Camera and Spectrograph (FOCAS; Kashikawa et al. 2002) on Subaru. Its Lyα line was measured to have FWHM = 900 ± 300 km s^{-1} and $L_{\mathrm{Ly}\alpha} \approx 10^{43.48}$ erg s^{-1} (Matsuoka et al. 2022). The classification of both sources was based on the onset of a prominent Lyα emission line and their blue continua. In the discovery spectrum of J1429−0104, a dip between the Lyα and N V lines was reported and interpreted as absorption associated with a broad absorption line (BAL) system (Matsuoka et al. 2018a).

A summary of the basic properties of J1429−0104 and J1450−0144 is presented in Table 1. Note that we have updated the redshifts using the [C II] line from our ALMA observations (Sect. 3.3) and M_{1450} from our JWST/NIRSpec data (Sect. 2.2.2). In Fig. 1 we show the two galaxies in the redshift versus M_{UV} plane with these updated values.

2.2 JWST/NIRSpec observation

2.2.1 *Observations and data reduction*

Both sources were later observed with JWST as part of the General Observers (GO) program 9180 (PI: J. Hennawi) using JWST/NIRSpec fixed-slit (FS) mode with the G140H/F070LP and G235H/F170LP configurations. The aim of the program include measuring the cosmic reionisation history from the damping wing signatures on the spectra of 27 faint quasars at $6.5 < z < 7.7$. Twelve of the 27 targets are discovered by *Euclid* (Yang et al. 2026), while the remainder are drawn primarily from SHELLQs, with preference given to sources with existing ALMA coverage (see Sect. 2.3). These setups provide a spectral resolution of $R \sim 2700$ and a continuous wavelength coverage of 0.81–3.05 μm[1], with both S200A1 and S200A2 used to bridge the inter-detector gap. For the two sources presented in this work, these observations enable rest-frame coverage from Lyα to approximately 4000 Å. The total exposure times for J1429−0104 are 9103 s and 5194 s for the G140H and G235H setups, respectively, while those for J1450−0144 are 3268 s and 2480 s.

We reduced the JWST/NIRSpec fixed-slit data starting from the `_uncal` exposures retrieved from MAST, using the JWST calibration pipeline (v1.20.2; CRDS context `jwst_1464.pmap`). Stage 1 (`calwebb_detector1`) performed the standard detector-level calibration including the `clean_flicker_noise` correction to produce `_rate` files. Stage 2 (`calwebb_spec2`) carried out the 2D spectroscopic calibration, including the wavelength calibration, flat-fielding, pathloss corrections, skipping the default background subtraction, 1D extraction, and resampling steps. Instead, sky subtraction and spectral extraction were performed with a custom interface between the Stage 2 products and `PypeIt` (Prochaska et al. 2020). For each slit, 2D science images, inverse-variance maps, and bad-pixel masks were constructed from the pipeline calibration arrays, with a custom variance model propagated from the JWST Poisson and read-noise estimates and an empirical rescaling factor of 1.5. The sky was modelled directly from the slit using `PypeIt`'s global B-spline algorithm. Sources were identified on the sky-subtracted 2D images and extracted using optimal extraction (Horne 1986). The individual 1D spectra from separate exposures and disperser settings were coadded with `pypeit_coadd_1dspec` onto a common wavelength grid. The final 1D spectra are displayed in Fig. 2.

2.2.2 *Spectral modelling*

Before performing any measurements from the NIRSpec spectra we apply two preparatory steps: an absolute flux correction with Subaru photometry information, and the construction of a continuum model that is subsequently used for all line and equivalent-width measurements.

The apparent UV magnitudes measured directly from the NIRSpec spectra are $M_{1450}^{\mathrm{raw}} = -23.23$ for J1450−0144 and −22.68 for J1429−0104 (Table 1). Due to the potential slit-losses, we rescale each spectrum to match the Subaru/HSC y-band magnitudes from Matsuoka et al. (2018a, 2022), corresponding to multiplicative flux corrections of ≃ 1.2 for J1450−0144 and ≃ 2.0 for J1429−0104. The large correction factor for J1429−0104 is consistent with its

[1] For typical targets, the red end of the G140H/F070LP configuration is truncated at 1.27 μm because of second-order contamination. The targets in this work lie at $z > 6.5$ and therefore possess a strong IGM absorption trough blueward of Lyα. As a result, second-order contamination does not impact our observations, enabling continuous spectral coverage.

Table 1. Source properties. Coordinates are J2000. The systemic redshifts $z_{[\rm C\,II]}$ are measured from the ALMA [C II] 158 μm line (Sect. 3.3). The y-band magnitudes $y_{\rm AB}$ are taken from the SHELLQs photometry (Matsuoka et al. 2018a, 2022) and set the absolute flux scale of the NIRSpec spectra (Sect. 2.2.2). $M_{1450}^{\rm raw}$ is the absolute UV magnitude measured directly from the NIRSpec spectrum as observed through the slit, whereas M_{1450} is measured after rescaling the spectrum to the y-band photometry and is the value adopted throughout this work. The difference for J1429−0104 is substantial, consistent with its extended morphology (Sect. 3.1.6). The spectral slope β ($f_\lambda \propto \lambda^\beta$) is measured from the rescaled spectra as described in Sect. 3.1.1.

Source	R.A.	Dec.	$z_{[\rm C\,II]}$	$y_{\rm AB}$	$M_{1450}^{\rm raw}$	M_{1450}	β
J1450−0144	14:50:05.39	−01:44:38.9	6.6270 ± 0.0018	23.45 ± 0.08	−23.23 ± 0.02	−23.45 ± 0.08	−2.20 ± 0.09
J1429−0104	14:29:03.08	−01:04:43.4	6.7964 ± 0.0002	23.73 ± 0.09	−22.68 ± 0.01	−23.45 ± 0.09	−2.06 ± 0.07

extended morphology (see Sect. 3.1.6). The rescaled spectra, which give the adopted $M_{1450} = -23.45$ for both sources, are used for all subsequent measurements. We note that the HSC imaging was taken several years ago, so this rescaling attributes the entire offset to aperture losses, ignoring any intrinsic variability between the two epochs. Future JWST/NIRCam imaging would help clarify this issue.

We model the rest-frame UV/optical continuum as a smoothing cubic spline (`scipy.interpolate.UnivariateSpline`), fit directly to the inverse-variance-weighted JWST spectrum after masking out possible line features. The smoothing parameter is chosen empirically so that the reduced χ^2 over the line-free pixels is close to unity while keeping the model free of structure on the scale of individual emission features. Continuum uncertainties are propagated by repeating the fit on 500 Monte Carlo realisations of the spectrum, each generated by perturbing every pixel by a Gaussian draw from its noise vector. The best-fit continuum is taken as the median across realisations. We show the resulting continuum models, together with the per-pixel residuals, in Appendix B.

We fit the following emission lines: N IV] λ1486, He II λ1640, O III] λ1666, C III] λ1907, 1909, Mg II λ2796, 2804, [O II] $\lambda\lambda$3727, 3730, and [Ne III] $\lambda\lambda$3870, 3969 with the continuum-subtracted spectrum using `lmfit` (Newville et al. 2025). We fit with Gaussian line models with the line redshift, amplitude, and width as free parameters. The redshift is allowed to vary within $\Delta z = \pm 0.02$ of the systemic value ($z_{[\rm CII]}$). For known doublets (N IV], O III], C III], Mg II, [O II]), we fit with two Gaussians with a shared σ and redshift but independent amplitudes. All derived FWHMs are deconvolved from the line-spread function assuming a Gaussian instrumental profile with $R = 2700$. Uncertainties on all fitted quantities are estimated from 500 Monte Carlo realisations in which the science spectrum is perturbed by its per-pixel error and refit with the continuum held fixed. We quote the 16th and 84th percentiles of the resulting distributions as the asymmetric 1σ errors. The best-fit models are displayed in Fig. 4 and the measurements are shown in Table 2.

2.3 ALMA observations

These two sources were also observed by ALMA in the cycle-10 program CISTERN ([C II]-SelecTed Early universe RefereNce, PI: Bouwens; Bouwens et al. 2026, in prep), targeting the [C II]$_{158\mu m}$ line from 92 *UV*-bright sources with spectroscopic redshifts. The integration time for J1429−0104 and J1450−0144 were 5.0 minutes and 5.5 minutes, respectively, yielding a line sensitivity of 0.5 mJy beam^{-1} per 66 km s^{-1} channel and a continuum sensitivity of 73 μJy beam^{-1}. This enables the detection of [C II] ISM cooling lines at 5σ down to luminosities of $\sim 4\times10^8\ L_\odot$ (corresponding to star-formation rates of 40 $M_\odot$ yr^{-1} based on the De Looze et al. (2014) SFR–L$_{[\rm CII]}$ relation). A synthesized beam size larger than 0.9″ was requested to avoid resolving out the typically extended [CII] emission observed in luminous star-forming galaxies and quasars at $z \gtrsim 6$. Additional details on the observations and source-by-source results will be presented in the forthcoming CISTERN survey paper (R.J. Bouwens et al. 2026, in prep.).

The ALMA data for each target were processed as follows. Measurement sets were generated from the QA2 delivery products using the ScriptForPI.py script within CASA (CASA Team et al. 2022). The visibilities were averaged in 30-second intervals and subsequently reimaged with the TCLEAN task using natural weighting. This weighting scheme maximizes the signal-to-noise ratio achievable for both line and continuum detections in CISTERN, providing a modest improvement relative to the standard JAO reductions, which adopt a Briggs weighting with a ROBUST parameter of 0.5. For continuum measurements, frequency ranges within ±0.4 GHz of any candidate ($>5\sigma$) [CII] line detections were excluded when generating continuum images of the targeted quasars.

We determine the systemic redshifts of J1450−0144 and J1429−0104 from the [C II] 158 μm line detected in our ALMA observations, with values reported in Table 1. Details of the [C II] line measurement are given in Sect. 3.3 and Appendix A.

3 RESULTS AND ANALYSIS

3.1 Nature of these two sources: Extreme UV Luminous Galaxies (EUVLGs) at cosmic dawn

With the JWST/NIRSpec spectra in hand, we are now in a position to revisit the nature of J1450−0144 and J1429−0104. Fig. 2 shows the G140H+G235H spectra of both sources, covering rest-frame wavelengths from Lyα to $\sim$ 4000 Å. Despite their quasar-like UV luminosities ($M_{1450} \approx -23.5$), neither spectrum resembles that of a typical type-I quasar. Instead, both display the hallmark features of EUVLG population, including blue UV continua, prominent P Cygni profiles in high-ionisation wind lines (N V λ1240, Si IV λ1400, and C IV λ1550, N IV λ1719), broad He II λ1640 emission, and strong narrow nebular lines (e.g., [O II] $\lambda\lambda$3727, 3730, [Ne III] $\lambda\lambda$3870, 3969). To make this comparison straightforward, Fig. 3 shows the Lyα to He II portion of each spectrum normalised by the local continuum, overlaid with the cosmic-noon EUVLG composite of Upadhyaya et al. (2024) (top) and the stacked spectrum of the seven most massive stars ($M_{\rm init} \sim 100 - 300\, M_\odot$) in R136 from Crowther et al. (2016) (bottom). Both J1450−0144 and J1429−0104 closely match the EUVLG composite and resemble the composite spectrum of the seven very massive stars in the R136. The P Cygni wind profiles in the high-ionisation resonance lines recall classical Wolf–Rayet (WR) stars. They are evolved massive stars whose dense, radiatively driven winds have stripped the hydrogen envelope to expose core-helium-burning layers. The features here, however, are not those of classical WR: as in R136, the strong broad He II, together with the P Cygni lines, point instead to the H-rich WR stars, usually denoted as the

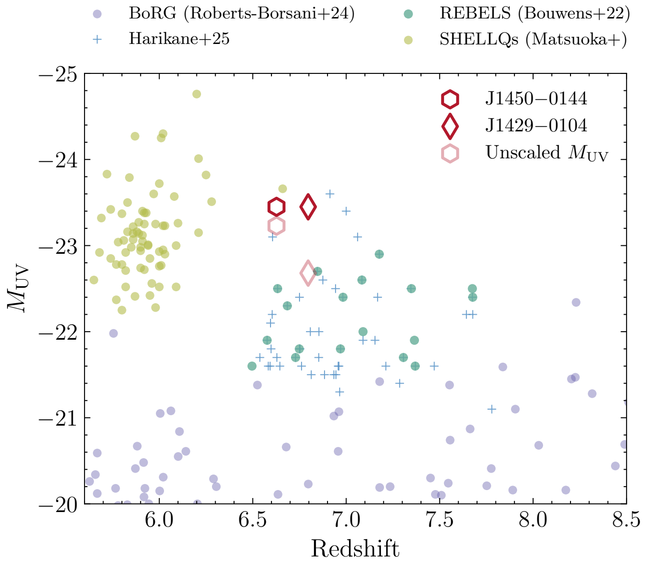

Figure 1. The two galaxies presented in this work (red) in the z–$M_{\rm UV}$ plane, compared with literature samples at $z \sim 6$–8.5: SHELLQs galaxies (Matsuoka et al. 2016, 2018a,b, 2019, 2022), REBELS galaxies (Bouwens et al. 2022), compilation samples in Harikane et al. (2025), and BoRG-JWST galaxies (Roberts-Borsani et al. 2024, 2025). Our sources lie among the UV-brightest spectroscopically confirmed galaxies known at $z > 6.5$.

WNh subclass. These stars are luminous hydrogen-rich stars close to the Eddington limit whose dense winds produce a WR-like emission spectrum while they still burn hydrogen in their cores, i.e. they are still in the main sequence. Both the P Cygni profiles and the broad He II emission arise in these winds, but only the resonance lines (N V, Si IV, C IV, N IV) develop the blueshifted P Cygni absorption, whereas the non-resonant He II appears predominantly in emission and only occasionally as a P Cygni profile. As suggested by many works (e.g., Vink et al. 2015; Crowther et al. 2016), very massive stars on the main sequence appear spectroscopically as WNh stars, so these features are hinting that VMS contribute substantially to the UV spectra, which we develop further in Sect. 3.2.3 and 4.2.

Finally, with the updated redshifts (Sect. 3.3) and rest-frame UV magnitudes ($M_{1450} \approx -23.5$), they sit among the UV-brightest spectroscopically confirmed galaxies known at $z > 6.5$, as shown in Fig. 1. These UV luminosities correspond to unobscured star-formation rates of $\mathrm{SFR_{UV}} \simeq 135 \pm 10\, M_\odot\,\mathrm{yr^{-1}}$ for both sources, adopting $\kappa_{\rm UV} = 1.3 \times 10^{-28}\,\mathrm{M_\odot\,yr^{-1}/(erg\,s^{-1}\,Hz^{-1})}$ from Upadhyaya et al. (2024), derived for the young stellar populations of cosmic-noon EUVLGs. However, as shown by Schaerer et al. (2025), for such young populations, and especially when VMS are present, $\kappa_{\rm UV}$ is a strong function of stellar age, declining by roughly an order of magnitude from $\simeq 10 \times 10^{-28}$ at ~ 1 Myr to $\simeq 1 \times 10^{-28}$ after ~ 10 Myr of constant star formation. The $\mathrm{SFR_{UV}}$ reported here should therefore be regarded as a first-order estimate.

3.1.1 *Blue UV continua*

The rest-frame UV continua of both J1450−0144 and J1429−0104 are blue and approximately power-law. We characterise the continuum slope by fitting $f_\lambda \propto \lambda^\beta$ to four line-free windows centred at rest-frame 1300, 1450, 1600, 1860 Å (each 20 Å wide), obtaining $\beta = -2.20 \pm 0.09$ for J1450−0144 and $\beta = -2.06 \pm 0.07$ for J1429−0104 (Table 1). Both slopes are consistent with young, star-forming galaxies. We note, however, that the observed UV slope of such a population is not set by the stellar continuum alone: nebular continuum emission (primarily two-photon and bound-bound) can redden the intrinsic slope by $\Delta\beta \sim 0.3$–0.6 at the youngest ages (Schaerer et al. 2025), an effect that becomes important precisely in the young-burst regime relevant here. The SED fitting we present in Sect. 3.2 does not include a separate nebular-continuum component. Dust attenuation and nebular reddening are therefore partially degenerate in the inferred $E(B-V)$, and the values quoted there should be regarded as upper limits on the true stellar dust attenuation. For context, the cosmic-noon EUVLG sample of Upadhyaya et al. (2024) has $\langle\beta\rangle = -2.33$. J1450−0144 and J1429−0104 sit at the redder end of this distribution but well within its spread.

Table 2. Emission-line properties measured from Gaussian fits to the continuum-subtracted JWST/NIRSpec spectra (Sect. 3.1.4). Lines marked with † are fitted as doublets (see Sect. 2.2.2). Their $\log L$ and $\mathrm{EW_0}$ are summed over both components, while FWHM and Δv are shared. The [Ne III] λ3969 line (marked with ‡) is blended with Hϵ λ3971 and fitted as a single Gaussian, the fitted values therefore absorb the Hϵ contribution.

Line	FWHM (km s^{-1})	$\log L$ (erg s^{-1})	EW$_0$ (Å)	Δv (km s^{-1})
J1450−0144				
N IV] λ1486†	1477^{+209}_{-825}	$42.42^{+0.06}_{-0.13}$	$1.9^{+0.3}_{-0.5}$	$+653^{+0}_{-602}$
He II λ1640	1906^{+119}_{-135}	$42.96^{+0.02}_{-0.03}$	$8.1^{+0.5}_{-0.5}$	$+227^{+51}_{-53}$
O III] λ1666†	813^{+91}_{-218}	$42.16^{+0.09}_{-0.08}$	$1.3^{+0.3}_{-0.2}$	-509^{+846}_{-18}
C III] λ1909†	1270^{+485}_{-552}	$42.41^{+0.10}_{-0.12}$	$3.2^{+0.8}_{-0.8}$	-294^{+243}_{-144}
Mg II λ2800†	527^{+44}_{-66}	$42.21^{+0.05}_{-0.05}$	$4.8^{+0.5}_{-0.5}$	-10^{+48}_{-56}
[O II] λ3728†	666^{+67}_{-96}	$42.63^{+0.03}_{-0.03}$	$25.7^{+1.8}_{-2.0}$	-67^{+37}_{-13}
[Ne III] λ3870	508^{+68}_{-70}	$42.40^{+0.04}_{-0.04}$	$13.9^{+1.5}_{-1.3}$	$+21^{+25}_{-30}$
[Ne III] λ3969‡	657^{+113}_{-134}	$42.20^{+0.07}_{-0.08}$	$11.1^{+1.9}_{-1.8}$	$+151^{+58}_{-68}$
J1429−0104				
N IV] λ1486†	2126^{+863}_{-1745}	$42.17^{+0.17}_{-0.18}$	$1.0^{+0.5}_{-0.3}$	-19^{+420}_{-393}
He II λ1640	2193^{+149}_{-194}	$42.69^{+0.04}_{-0.04}$	$4.0^{+0.4}_{-0.4}$	$+520^{+106}_{-108}$
O III] λ1666†	456^{+32}_{-327}	$41.76^{+0.12}_{-0.13}$	$0.5^{+0.2}_{-0.1}$	$+105^{+71}_{-102}$
C III] λ1909†	1322^{+204}_{-149}	$42.57^{+0.05}_{-0.06}$	$4.0^{+0.5}_{-0.5}$	$+92^{+107}_{-113}$
Mg II λ2800†	192^{+28}_{-23}	$42.17^{+0.07}_{-0.05}$	$3.8^{+0.6}_{-0.4}$	$+102^{+17}_{-16}$
[O II] λ3728†	364^{+19}_{-21}	$42.85^{+0.01}_{-0.02}$	$34.1^{+1.2}_{-1.3}$	$+36^{+10}_{-10}$
[Ne III] λ3870	328^{+22}_{-21}	$42.68^{+0.02}_{-0.02}$	$27.5^{+1.5}_{-1.2}$	$+118^{+8}_{-8}$
[Ne III] λ3969‡	491^{+41}_{-44}	$42.53^{+0.04}_{-0.04}$	$22.8^{+2.0}_{-1.9}$	$+213^{+23}_{-23}$

3.1.2 *P Cygni wind profiles*

Both sources show prominent P Cygni profiles in the high-ionisation lines N V λ1240, Si IV λ1400, and C IV λ1550, each consisting of a blueshifted absorption trough and a redshifted emission peak at the systemic redshift (Fig. 3). P Cygni profiles in these resonance lines are the canonical signature of radiatively driven winds from massive OB stars (e.g., Vink et al. 2001), with their strength enhanced by Wolf–Rayet-like outflows near the Eddington limit (e.g., Crowther 2007; Crowther et al. 2016).

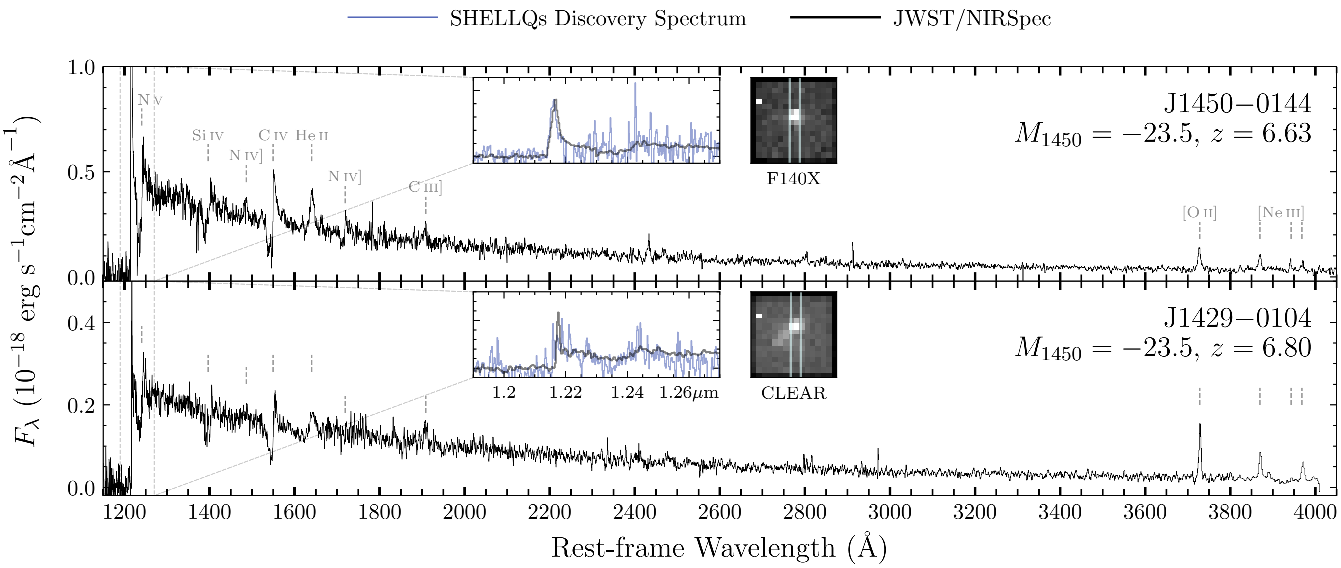

Figure 2. JWST/NIRSpec of J1450−0144 (top, $z = 6.63$) and J1429−0104 (bottom, $z = 6.80$), covering ∼1200–4000 Å in rest-frame. Black curves show the JWST/NIRSpec G140H+G235H spectra, blue curves in the inset show the original SHELLQs discovery spectra from GTC/OSIRIS and Subaru/FOCAS, respectively (Matsuoka et al. 2018a, 2022). Both sources exhibit the characteristic features of extreme UV-luminous star-forming galaxies: blue UV continua, prominent P Cygni profiles in the high-ionisation wind lines N v λ1240, Si iv λ1400, and C iv λ1550, broad He ii λ1640 emission, absence of broad Lyα and Mg ii, and narrow nebular lines including [O ii] $\lambda\lambda$3727, 3730 and [Ne iii] $\lambda\lambda$3870, 3969. The inset images on the right show the NIRSpec WATA stamps (1.6″ × 1.6″) obtained with the F140X filter (J1450−0144) and CLEAR filter (J1429−0104). J1429−0104 shows extended morphology.

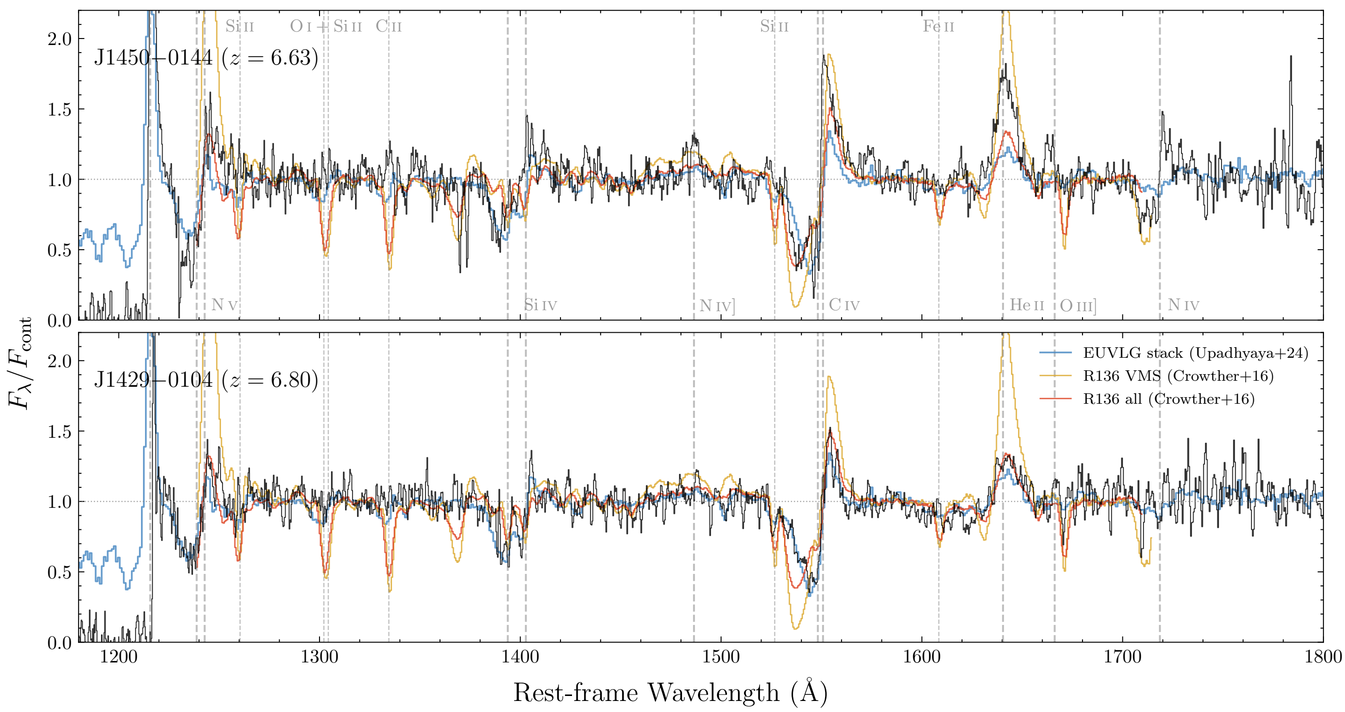

Figure 3. Rest-frame UV spectra of J1450−0144 (top; $z = 6.63$) and J1429−0104 (bottom; $z = 6.80$), each overlaid with the cosmic-noon EUVLG composite of Upadhyaya et al. (2024) (blue), the stacked spectrum of the seven most massive stars ($M_{\mathrm{init}} \sim 100$–$300\,M_\odot$) in the R136 cluster (yellow) and the entire R136 (red) from Crowther et al. (2016). Black curves show the JWST/NIRSpec spectra for the two galaxies, smoothed with an inverse-variance-weighted 3-pixel window. All spectra are normalised by the local UV continuum. Key high-ionisation wind and nebular features are labelled. Both reionisation-epoch galaxies closely resemble the cosmic-noon EUVLG composite and the R136 VMS spectrum across the high-ionisation P Cygni lines. See Sect. 3.1 for further discussion.

The C IV and N V profiles are particularly strong, with absorption components reaching $F_\lambda/F_{\rm cont} \sim 0.2$–0.5 and comparably prominent emission peaks. In J1450−0144 we also identify a clear N IV λ1719 P Cygni profile. Compared with the cosmic-noon EUVLG composite of Upadhyaya et al. (2024) (blue in Fig. 3), J1429−0104 matches the composite closely in all three P Cygni profiles, while J1450−0144 shows systematically stronger N V, Si IV, and C IV features; the N IV P Cygni profile is not seen in the cosmic-noon composite. Compared with the R136 VMS stack of Crowther et al. (2016) (red), the C IV P Cygni profiles in both sources match R136 closely in depth and shape, but R136 shows a substantially stronger N V emission component than either galaxy. Conversely, P Cygni Si IV is absent in the R136 stack yet present in both of our sources. Crowther et al. (2016) attribute the absence of Si IV λ1400 P Cygni emission to a lack of mid- to late-type O supergiants.

The strength and consistency of the profiles observed here imply a young stellar population in which radiatively driven winds dominate the rest-UV resonance-line spectrum, and the systematically stronger P Cygni profiles in J1450−0144 relative to J1429−0104 are consistent with a younger age, since wind-line strengths peak in the first ~ 2 Myr of a starburst. We model both populations quantitatively in Sect. 3.2.

The P Cygni morphology of J1450−0144 and J1429−0104 further rules out a broad absorption line (BAL) quasar origin, a class of object that can sometimes superficially mimic a starburst spectrum at low spectral resolution (Appenzeller et al. 2005). The crucial distinction is that each of the three high-ionisation absorption features in our spectra is accompanied by a redshifted emission component anchored at the systemic redshift, producing the symmetric P Cygni morphology characteristic of stellar winds. BAL outflows, by contrast, produce only the blueshifted absorption component, typically offset by thousands of km s^{-1} from systemic and without a compensating emission peak. The bona fide P Cygni nature of the profiles in J1450−0144 and J1429−0104 is further confirmed by the population-synthesis fits in Sect. 3.2 (also see Fig. 6 and 7), which reproduce both the blueshifted absorption and the redshifted emission of each line consistently.

3.1.3 *Broad He II and other wind-line features*

In addition to the P Cygni profiles described above, several emission features in J1450−0144 and J1429−0104 are significantly broader than the narrow nebular lines (FWHM $\lesssim$ 1200 km s^{-1}) and likely originate from the optically-thick stellar winds (e.g., Martins & Palacios 2022; Martins et al. 2025), including N IV] λ1486, He II λ1640, and C III] λ1909. They are shown in Fig. 4, and the Gaussian-fit results are listed in Table 2. The He II emission is remarkably strong, with FWHM $\sim$ 1900–2200 km s^{-1} and rest-frame equivalent widths $\mathrm{EW}_0 = 8.1 \pm 0.5$ Å in J1450−0144 and 4.0 ± 0.4 Å in J1429−0104. The strength of the He II in J1450−0144 is comparable with the seven most massive stars in R136 and the one for J1429−0104 is comparable to the cosmic-noon EUVLG stack, as can be seen from Fig. 3, placing both galaxies among the strongest broad-He II emitters known in star-forming galaxies and pointing to a substantial population of very massive stars. In Sect. 4.2 we inspect the VMS content based on the He II strength. To compare directly with cosmic-noon EUVLG measurements in Upadhyaya et al. (2024), we there adopt EW_0 measured by direct integration of the continuum-subtracted flux rather than the Gaussian-fit values. The two measurements are consistent within the uncertainties, with the non-parametric $\mathrm{EW}_0 = 8.8 \pm 1.2$ and 3.7 ± 1.1 Å for He II in J1450−0144 and J1429−0104, respectively. For N IV] λ1486, J1450−0144 has a strong detection with $\mathrm{EW}_0 = 1.9^{+0.3}_{-0.5}$ Å and FWHM $= 1477^{+209}_{-825}$ km s^{-1}, while for J1429−0104 it is only marginal ($\mathrm{EW}_0 = 1.0^{+0.5}_{-0.3}$ Å), with a poorly constrained width (FWHM $= 2126^{+863}_{-1745}$ km s^{-1}). The semi-forbidden line C III] λ1909 is usually taken to be of nebular origin, but here it also exceeds the typical nebular limit, with FWHM $\sim$ 1300 km s^{-1} and $\mathrm{EW}_0 \approx$ 3–4 Å in both sources, suggesting a partial stellar-wind contribution to the total emission.

The widths of these lines rules out a purely nebular origin, and a quasar broad-line region (BLR) is also disfavored for several reasons. First, if these lines were produced in a BLR, the resonant Lyα line should appear as a strong, broad feature at least as broad as He II. Instead, no broad Lyα is seen in either source (Figs. 2 and 3). Second, the high-ionisation resonance lines C IV λ1549 and N V λ1240 show P Cygni profiles (Sect. 3.1.2) rather than the symmetric broad emission expected from a BLR, or a broad absorption trough as in BAL. Their blueshifted absorption troughs are a characteristic feature of expanding stellar winds, not photoionised BLR gas. Third, the Mg II $\lambda\lambda$2796, 2804 doublet is detected with a narrow width (FWHM $\sim$ 200–500 km s^{-1}; see Table 2 and Sect. 3.1.4), consistent with nebular rather than BLR gas. The broad lines are therefore most naturally produced in the dense, radiatively driven winds of young massive stars, whose terminal velocities set the line widths and whose mass-loss rates and wind densities set the equivalent widths.

3.1.4 *Narrow nebular emission lines*

In contrast to the broad wind-driven features discussed above, both spectra also show narrow emission lines characteristic of photoionised gas. Fig. 4 shows close-up views of the individual lines, and Table 2 summarises the measured properties. Details of the continuum modelling and Gaussian fitting are given in Appendix B. The forbidden lines [O II] $\lambda\lambda$3727, 3730 and [Ne III] $\lambda\lambda$3870, 3969 are detected at high significance ($\gtrsim 5\sigma$) in both sources, with FWHM $\sim$ 330–670 km s^{-1}. The cosmic-noon EUVLG sample shows similarly narrow nebular emission whose line ratios favour photoionisation by young stars over AGN activity (e.g., Marques-Chaves et al. 2022). Our current wavelength coverage does not extend to the rest-frame optical diagnostic lines (Hα, [O III] $\lambda\lambda$4959, 5007, [N II] $\lambda\lambda$6548, 6584) needed to confirm this directly, but the close spectral similarity in the rest-frame UV suggests analogous excitation conditions.

Using the [Ne III]/[O II] ratio (Ne3O2) as a metallicity indicator, we obtain log(Ne3O2) ≈ -0.17 for both sources. Applying the high-redshift empirical calibration of Sanders et al. (2025) yields $12 + \log(\mathrm{O/H}) \approx 8.0$, corresponding to $Z \approx 0.2\,Z_\odot$ for a solar oxygen abundance of $12 + \log(\mathrm{O/H})_\odot = 8.69$ (Asplund et al. 2021). We adopt this metallicity when fixing the template grid in the SED fitting (Sect. 3.2). One caveat is that if EUVLGs are Lyman-continuum leakers, as suggested by Marques-Chaves et al. (2022), density-bounded H II regions could preferentially suppress low-ionisation lines such as [O II] and bias the Ne3O2-derived metallicity low. However, the Ne3O2 values we measure are not unusually elevated and fall well within the calibrated range, so we retain them as working estimates pending rest-frame optical follow-up.

3.1.5 *Weak low-ionisation interstellar absorption*

Equally notable is the lack of low-ionisation interstellar (LIS) absorption lines tracing the neutral ISM, such as Si II λ1260, O I λ1302 + Si II λ1304, C II λ1334, and Si II λ1526. They are not apparent in either galaxy at the current depth (Fig. 3). Unlike the high-ionisation wind features of Sect. 3.1.2, these transitions arise

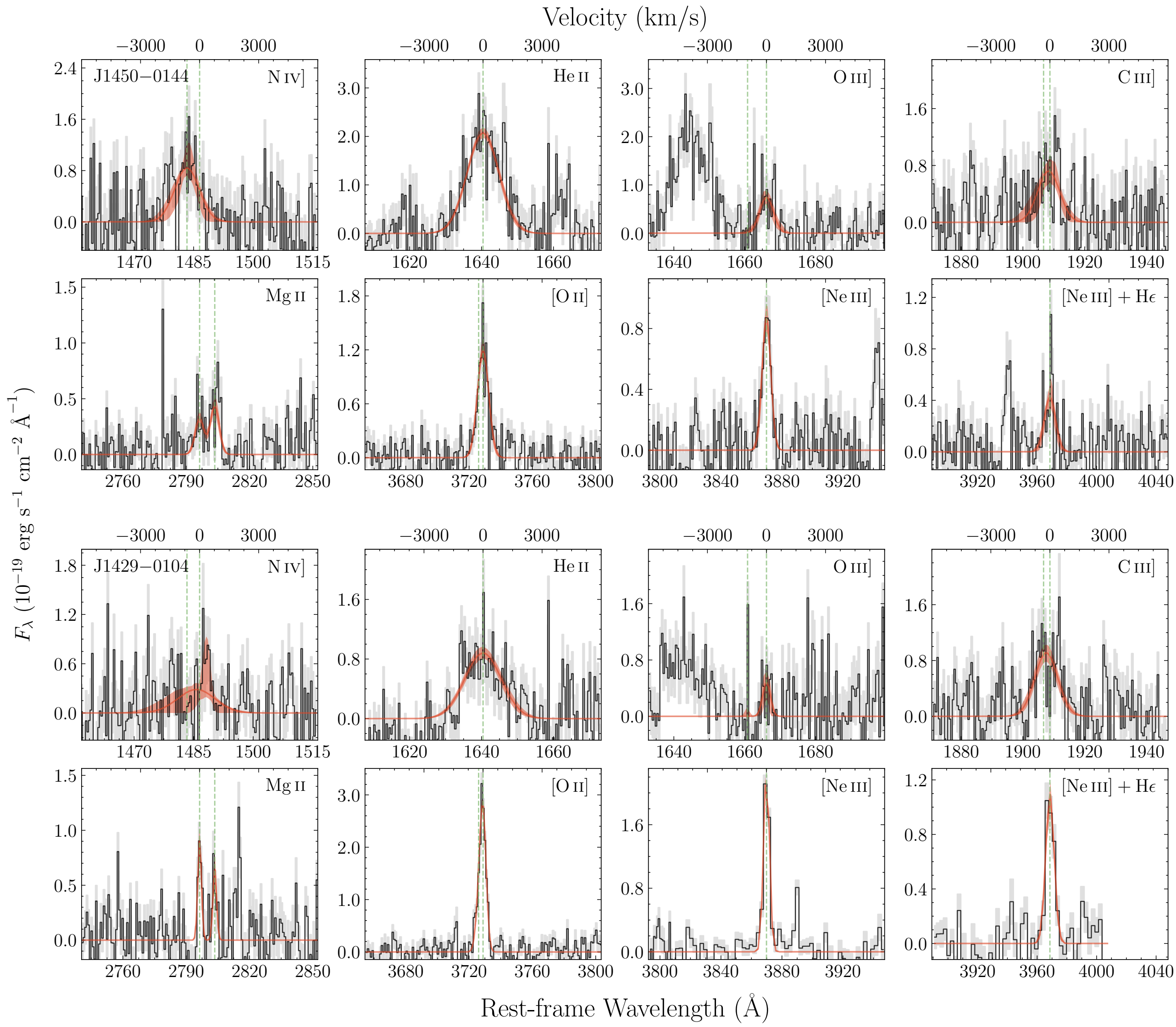

Figure 4. Continuum-subtracted data of the emission lines and their best-fit Gaussian (or double-Gaussian, for doublets) models in J1450−0144 (top two rows) and J1429−0104 (bottom two rows). From left to right and top to bottom in each block: N IV] $\lambda\lambda$1483, 1486, He II λ1640, O III] $\lambda\lambda$1661, 1666, C III] $\lambda\lambda$1907, 1909, Mg II $\lambda\lambda$2796, 2804, [O II] $\lambda\lambda$3727, 3730, [Ne III] λ3870, and [Ne III] λ3969. See Sect. 2.2.2 for details of the continuum modelling and line-fitting procedure. The resulting line measurements are reported in Table 2.

in neutral gas in the ISM along the line of sight, and in typical star-forming galaxies at $z \sim 2$–3 they appear with $EW_0 \sim 1$–2 Å (e.g., Shapley et al. 2003). Cosmic-noon EUVLGs span a wide range of LIS strengths, from clearly detected absorption in BOSS-EUVLG1 and J0121+0025 (Marques-Chaves et al. 2020, 2021) to undetected LIS lines in J1316+2614 (Marques-Chaves et al. 2022). Our two sources resemble the latter. Similarly weak interstellar absorption is also seen in the young, low-metallicity galaxy Q2343-BX418 at $z = 2.3$ (Erb et al. 2010), and the ultra-deep SPURS spectrum of GN-z11 at $z = 10.6$ likewise shows no detectable LIS absorption, interpreted as a low covering fraction of enriched neutral gas in front of its UV-emitting regions (Chen et al. 2026).

Because the LIS transitions are typically saturated, their depth measures the covering fraction of neutral gas rather than its column density, so their weakness signals a low H I covering fraction and favourable conditions for the escape of Lyman-continuum (LyC) photons (e.g., Reddy et al. 2016; Gazagnes et al. 2018; Saldana-Lopez et al. 2022). Among the cosmic-noon EUVLGs, the LIS strength indeed tracks the measured LyC leakage: J0121+0025, with detected LIS absorption, is a leaker with f_{esc}(LyC) ≈ 40 per cent, whereas J1316+2614, with no detectable LIS lines, leaks at f_{esc}(LyC) ≈ 90 per cent (Marques-Chaves et al. 2021, 2022). The strong, narrow Lyα emission that drove the original quasar classification of both sources (Sect. 2.1) fits naturally into the same picture, since Lyα escape is likewise regulated by the H I covering fraction, and a low covering fraction would also act in the same direction as the density-bounded scenario flagged in Sect. 3.1.4. We caution that this interpretation remains qualitative: the continuum signal-to-noise ratio limits the constraining power of the non-detections, the LIS lines may not be fully saturated at the relatively low metallicity, and for J1429−0104 any escape must be strongly direction dependent given the ∼ 5.4 kpc offset between its UV and dust/[C II] emission (Sect. 3.3). Quantitative constraints on the covering fraction and the escape of ionising radiation are deferred to future work.

3.1.6 Morphology

Finally, Fig. 2 also includes NIRSpec Wide Aperture Target Acquisition (WATA) images (1.6″ × 1.6″) of the two objects, taken with the F140X filter for J1450−0144 and the CLEAR filter for J1429−0104. J1450−0144 is consistent with a point source, unresolved at the ∼ 0.1″ FWHM of the WATA PSF, which corresponds to ∼ 500 pc at $z = 6.63$ and sets an upper limit on the size of the rest-frame UV emitting region. J1429−0104 also shows a bright, compact core on which the NIRSpec slit is centred, but additionally exhibits clearly extended structure to the south–east (see also Fig. 9). The compact component dominates the rest-frame UV light entering the slit and therefore drives the spectrum of J1429−0104. Whether the extended component traces the rest-frame UV or optical light is unclear, since the CLEAR configuration transmits the full NIRSpec range (∼ 0.6–5.3 μm) and so the image is sensitive to Lyα and to strong rest-frame optical lines such as [O III] λ5007. Higher-resolution imaging with JWST/NIRCam with multiple filters, or deep JWST/NIRSpec IFU observations, are needed to characterise the detailed morphologies and individual components of both galaxies.

3.2 Young, star-forming stellar populations

The same UV wind signatures, blue continua, and nebular-line-dominated emission seen in cosmic-noon EUVLGs support the interpretation that the extreme UV luminosities of our two sources are powered primarily by young stars rather than by AGN activity. We therefore infer their stellar populations by fitting the rest-frame UV P-Cygni wind features with stellar population synthesis (SPS) models. These features arise in the radiatively driven winds of short-lived massive stars ($\lesssim$ 10 Myr for $M \gtrsim 15\,M_\odot$). Both their presence and their relative strength evolve rapidly over the first few Myr of star formation, which makes them sensitive diagnostics of the recent star-formation history.

However, as shown in Sect. 3.1.3, both galaxies exhibit strong broad He II λ1640 emission, with equivalent widths well above those of typical star-forming galaxies. Cosmic-noon EUVLGs show similarly strong He II, which has been attributed to the presence of very massive stars (Upadhyaya et al. 2024). Canonical SPS models typically truncate the IMF at $M_{\rm up}$ = 100–120 M$_\odot$ and lack dedicated VMS atmosphere and wind models, and may therefore be unable to reproduce the observed spectra. In Sect. 3.2.1 we describe the two sets of SPS models we use: standard `BPASS` models and their extension with dedicated VMS treatment from Upadhyaya et al. (2024). We present the fitting results with the standard models in Sect. 3.2.2 and with the VMS extension in Sect. 3.2.3.

3.2.1 Population synthesis models and fitting method

The first family is the standard `BPASS` v2.2.1 binary grid (Eldridge et al. 2017; Stanway & Eldridge 2018), which adopts a broken power-law IMF ($\alpha = -1.30$ below 0.5 M$_\odot$ and $\alpha = -2.35$ above) with upper-mass limits of 100 and 300 M$_\odot$. Following Upadhyaya et al. (2024), we convert the native 10^6 M$_\odot$ instantaneous-burst spectra to a constant star-formation rate (CSFR) of 1 M$_\odot$ yr^{-1} by summing the burst spectra over the native BPASS age bins. The grid is sampled at nominal $\log(t/{\rm yr})$ = 6.0–8.0 in steps of 0.1. We fix the metallicity at $Z = 0.006$, matching the metallicity of the `BPASS+VMS` models introduced next. This is higher than the $Z = 0.004$ suggested by the Ne3O2 ratio in Sect. 3.1.4, but the difference has small effect on the fitted parameters. We therefore adopt $Z = 0.006$ for consistency with the `BPASS+VMS` models, which are available only at this metallicity. Hereafter, we refer to this model family as `BPASS-only`.

The second family is the `BPASS+VMS` grid from Upadhyaya et al. (2024), which augments `BPASS` v2.2.1 with the VMS models of Martins & Palacios (2022) and extends the IMF to five upper-mass limits between $M_{\rm up}$ = 175 and 475 M$_\odot$. The VMS models adopt the Gräfener (2021) mass-loss prescription for stars near the Eddington limit, which Martins & Palacios (2022) showed is required to reproduce the strong broad He II emission of the VMS in R136 (Crowther et al. 2016). We return to this in Sect. 4.2.3. The grid adopts a Salpeter IMF ($\alpha = -2.35$), identical to the standard grid above 0.5 M$_\odot$. The difference below this mass is irrelevant for the rest-UV spectrum. We also use models with CSFR, sampled at $\log(t/{\rm yr})$ = 6.0–8.0 in steps of 0.1. This choice is mainly because of the short lifetimes of VMS, i.e. in a burst model, all VMS die within a few Myr, and the models lose their constraining power on $M_{\rm up}$.

We fit both families with the same procedure. Rather than fitting the absolute-flux spectrum, we compare continuum-normalised line profiles in three rest-frame windows: 1230–1245 Å (N V), 1530–1560 Å (C IV), and 1630–1655 Å (He II). The observed spectrum is normalised by the spline continuum of Sect. 2.2.2, with the continuum uncertainty propagated into the normalised errors, and each model is normalised by the median flux in flanking line-free sidebands. Both dust attenuation and the absolute flux calibration cancel in normalised space, so the fit has no free scale or reddening parameter: we compute χ^2 over all pixels in the three windows, constraining the burst age for the standard grid and the duration of star formation and $M_{\rm up}$ for the `BPASS+VMS` grid. We subsequently estimate $E(B{-}V)$ by reddening the best-fit template with the Calzetti et al. (2000) law ($R_V = 4.05$) until its UV slope matches the observed β. Parameter uncertainties are derived from the χ^2 grid by weighting each template by $\exp(-\Delta\chi^2/2)$, rescaling $\Delta\chi^2$ by the minimum reduced χ^2 where it exceeds unity, and quoting the median and 16th–84th percentile interval.

3.2.2 `BPASS-only` models fail to produce the broad He II emission in these two galaxies

Figs. 6 and 7 show the best-fit `BPASS-only` templates for J1450−0144 and J1429−0104 (blue curves), with the corresponding parameters summarised in Table 3. The `BPASS-only` models favour very young stellar populations in both galaxies, with best-fit ages of 2.0 Myr for J1450−0144 and 4.0 Myr for J1429−0104, and mild reddening of $E(B-V) \simeq 0.1$. Scaling each reddened best-fit template to the observed flux yields SFR $\simeq$ 990 and $\simeq 590\,M_\odot$ yr^{-1} for J1450−0144 and J1429−0104, respectively, and under the constant star-formation history assumed here the stellar masses follow as $\log(M_\star/M_\odot)$ = 9.29 and 9.37.

These young stellar populations reproduce the prominent N V and C IV P-Cygni features reasonably well. The fits fail, however, at He II. All models in the grid substantially underpredict the observed strength of the observed broad He II emission, with EW$_0$ = 8.8 ± 1.2 Å for J1450−0144 and 3.7 ± 1.1 Å for J1429−0104 (Sect. 3.1.3). Between the two available upper-mass limits, both fits favour $M_{\rm up} = 300\,M_\odot$ over 100 $M_\odot$, yet even these models fall well short of the observed He II. Extending the IMF above 100 $M_\odot$ therefore does not by itself produce the observed emission.

Broad stellar He II emission in typical star-forming galaxies has EW$_0$ of order 1–2 Å (e.g., Shapley et al. 2003; Steidel et al. 2016) and is generally attributed to the winds of classical Wolf–Rayet (cWR) stars (Schaerer & Vacca 1998; Brinchmann et al. 2008). Individual cWR stars can show strong He II emission formed in their dense,

Table 3. Summary of stellar population parameters inferred from template fitting (Sect. 3.2.1). Metallicities are fixed at $Z = 0.006$ ($Z/Z_\odot = 0.3$ with $Z_\odot = 0.02$). All models assume a constant star-formation history, and the age column denotes the duration of star formation. The SFR is obtained by scaling each best-fit template, reddened with its $E(B-V)$, to the observed flux level, and the stellar mass follows as $M_\star$ = SFR × age.

Template	Age (Myr)	$E(B-V)$	$\log(M_\star/M_\odot)$	$M_{\rm up}$ ($M_\odot$)	SFR ($M_\odot$/yr)
		J1450−0144			
`BPASS-only`	2.00	0.10	9.29	300	986.42
`BPASS+VMS`	3.16	0.09	9.24	275	543.71
		J1429−0104			
`BPASS-only`	3.98	0.12	9.37	300	594.91
`BPASS+VMS`	25.12	0.11	9.88	325	299.50

optically thick winds (Crowther 2007; Martins et al. 2023), but they constitute only a small fraction of the massive-star population, while the integrated UV continuum is dominated by the far more numerous OB stars. Their contribution is therefore heavily diluted in galaxy-integrated spectra, and the `BPASS-only` models, which include these cWR phases, accordingly predict He II at this modest level (see also Upadhyaya et al. 2024). The much stronger broad He II in J1450−0144 and J1429−0104 points to a massive-star population not captured by the `BPASS-only` models.

3.2.3 *BPASS+VMS models successfully produce the broad He II emission*

Figs. 6 and 7 also show the best-fit `BPASS+VMS` templates (red curves), with the corresponding parameters summarised in Table 3. The best-fit models have $M_{\rm up} = 275\,M_\odot$ with an age of 3.2 Myr for J1450−0144, and $M_{\rm up} = 325\,M_\odot$ with an age of 25 Myr for J1429−0104, with reddening of $E(B-V) = 0.09$ and 0.11 and stellar masses of $\log(M_\star/M_\odot) = 9.24$ and 9.88, respectively. The same scaling yields SFR $\simeq 540$ and $\simeq 300\,M_\odot\,{\rm yr}^{-1}$ (Table 3). These rates exceed the $\mathrm{SFR_{UV}} \simeq 135\,M_\odot\,{\rm yr}^{-1}$ of Sect. 3.1 by factors of $\approx$ 2–4 for two reasons. The template-fitting SFRs should be regarded as total star-formation rate, whereas $\mathrm{SFR_{UV}}$ is the unobscured part. In addition, at the young ages found here the UV continuum has not yet built up to the equilibrium level assumed by a fixed $\kappa_{\rm UV}$, which could bias $\mathrm{SFR_{UV}}$ low (Schaerer et al. 2025). The notably older age and higher stellar mass of J1429−0104 relative to its `BPASS-only` fit are discussed below. These templates produce substantially stronger He II emission, while matching the N V and C IV P-Cygni profiles as well as the `BPASS-only` fits.

As mentioned in Sect. 3.2.2, simply extending the IMF above $M_{\rm up} = 100\,M_\odot$ is insufficient to reproduce the observed He II strength (see also Upadhyaya et al. 2024; Marques-Chaves et al. 2026). The strong He II emerges only when the models include the dedicated VMS atmospheres of Martins & Palacios (2022), which is based on the mass-loss prescription of Gräfener (2021) calibrated on the VMS observed in R136 in the LMC. The relevant ingredient is therefore not just the presence of stars above 100 $M_\odot$, but the distinct wind physics of very massive stars. At sufficiently high masses and luminosities, the increasing Eddington factor drives dense, optically thick winds (Vink et al. 2011; Gräfener et al. 2011; Bestenlehner et al. 2014), and these stars exhibit Wolf–Rayet-like spectra already on the main sequence, spectroscopically resembling the WNh stars (e.g., Crowther et al. 2010). Because they are also exceptionally luminous in the UV, even a small population contributes disproportionately to the integrated UV light of a young stellar population. Their wind signatures therefore become prominent in the galaxy-integrated spectrum, producing the strong N V and C IV P-Cygni profiles together with the broad He II emission observed in J1450−0144 and J1429−0104.

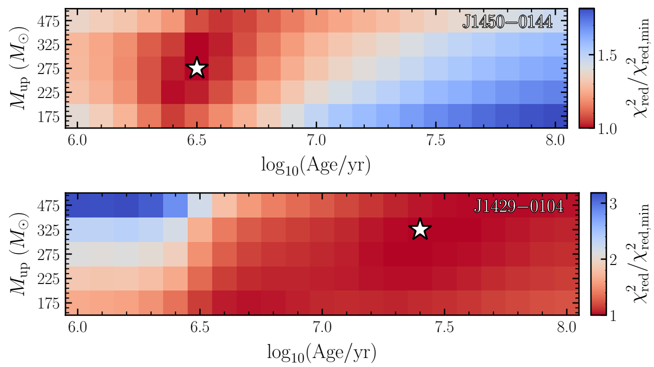

Figure 5. Goodness of fit for the BPASS+VMS template fitting of J1450−0144 (top) and J1429−0104 (bottom). The colour scale shows the reduced χ^2, normalised to its minimum over the grid, as a function of the age of the constant star-formation model and the IMF upper-mass limit $M_{\rm up}$, at fixed $Z = 0.006$. The χ^2 is evaluated over the N V, C IV, and He II windows defined in Sect. 3.2, and white stars mark the best-fit models. For J1450−0144 the fit prefers a young population with $\log(t/{\rm yr}) = 6.5$ and $M_{\rm up} = 275\,{\rm M_\odot}$. For J1429−0104 the surface is shallow at $\log(t/{\rm yr}) \gtrsim 6.5$, with a formal minimum at $\log(t/{\rm yr}) = 7.4$ and $M_{\rm up} = 325\,{\rm M_\odot}$, so the age is only weakly constrained, a younger population at $\log(t/{\rm yr}) \lesssim 7$ but lower $M_{\rm up}$ is also consistent with the data.

The best-fit `BPASS+VMS` template for J1450−0144 additionally shows broad N IV] λ1486 emission and a N IV λ1719 P-Cygni feature, and both features are present in the data. Martins & Palacios (2022) identify these as further characteristic signatures of very massive stars, lending additional support to the presence of a VMS population in J1450−0144.

The best-fit parameters of J1429−0104 are noticeably different from those in the `BPASS-only` fit. The `BPASS+VMS` model returns an age older by a factor of six and a stellar mass higher by 0.5 dex. To assess how well these parameters are actually constrained, Fig. 5 shows the reduced χ^2 over the age–$M_{\rm up}$ grid for both galaxies. For J1450−0144 the minimum is well localised at ages of 2–4 Myr, consistent with the `BPASS-only` result, because only very young populations with a substantial VMS contribution approach the observed strength of its wind features. For J1429−0104, in contrast, the χ^2 surface is shallow and the formal best fit carries little significance. Under a constant star-formation history the VMS population reaches a steady state within a few Myr, while the UV continuum from longer-lived stars continues to build, so the wind-line equivalent widths

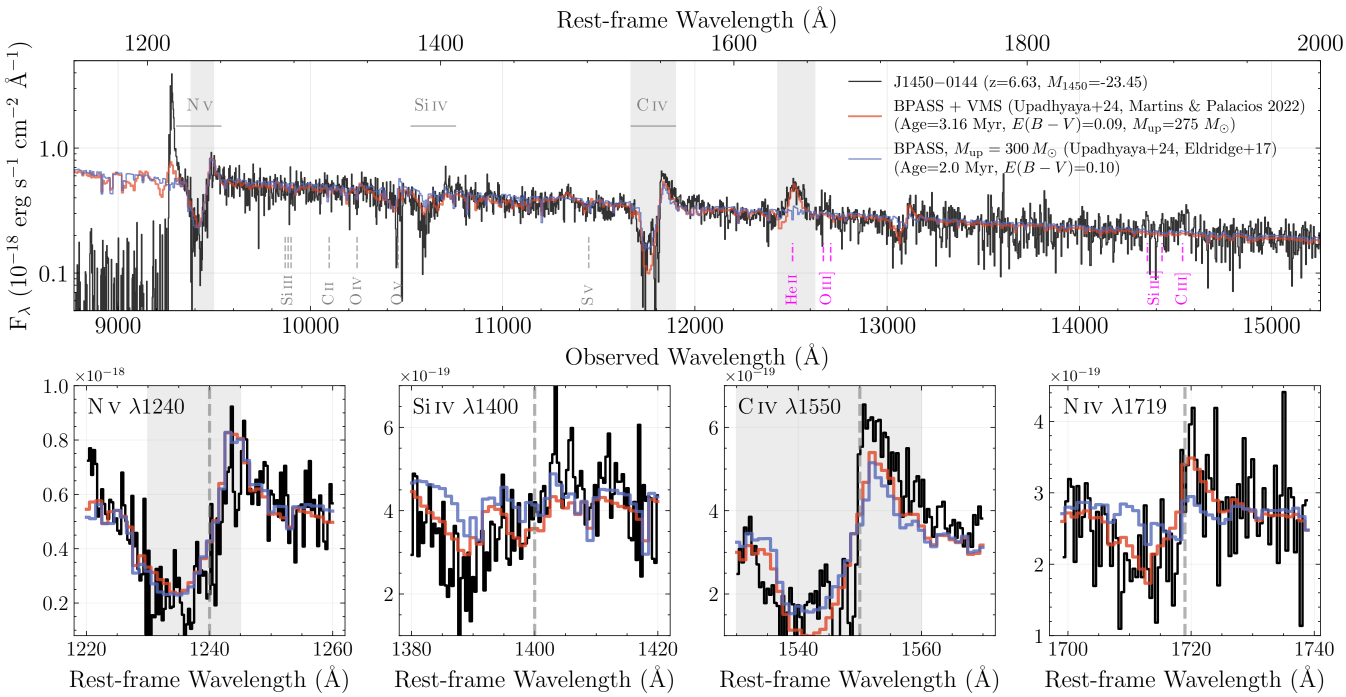

Figure 6. Stellar population fitting for J1450−0144. The upper panel shows the observed JWST/NIRSpec spectrum (black) compared with the best-fit `BPASS-only` (blue; Eldridge et al. 2017; Stanway & Eldridge 2018; Upadhyaya et al. 2024) and `BPASS+VMS` (red; Upadhyaya et al. 2024) templates, both under a constant star-formation history at fixed $Z = 0.006$. The best-fit star-formation durations (age), $E(B-V)$, and $M_{\rm up}$ are given in the legend and Table 3. Grey bands mark the three windows entering the continuum-normalised fit (N v, C iv, and He ii; Sect. 3.2.1). For display, each template is reddened with its best-fit $E(B-V)$ and scaled to the observed flux. The lower panels zoom in on the wind profiles N v λ1240, Si iv λ1400, C iv λ1550, and N iv λ1719, with the fitted pixels again shaded; Si iv and N iv λ1719 are shown for comparison but are excluded from the fit, and the He ii profiles are compared in Fig. 14.

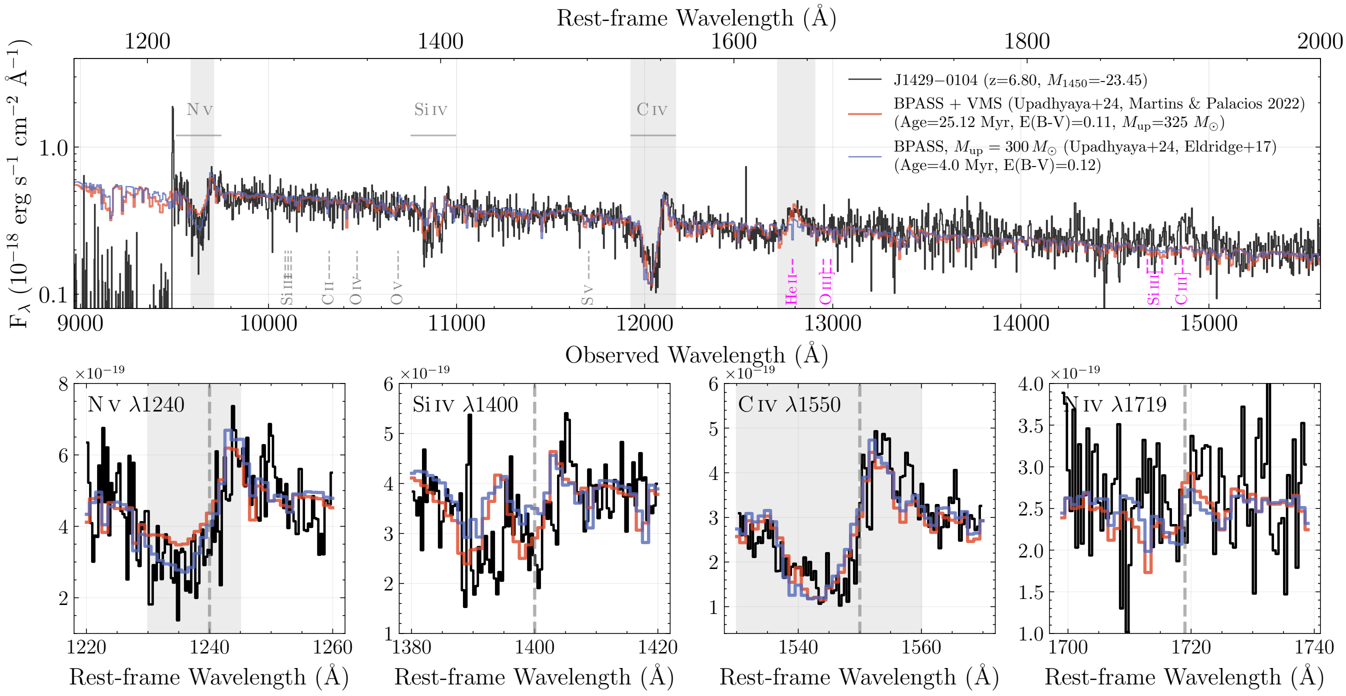

Figure 7. Stellar population fitting for J1429−0104, same as Fig. 6.

decline slowly with age; raising M_{up} increases them at all ages. The two parameters therefore compensate, and the moderate wind-line strengths of J1429−0104 are reproduced comparably well across most of the grid: a young population with a lower M_{up} and an older population with a higher M_{up} are indistinguishable at the current signal-to-noise ratio, and only the combination of ages $\lesssim 3$ Myr and $M_{up} \gtrsim 325\,M_\odot$ is excluded. The age and M_{up} of J1429−0104 are thus individually only weakly constrained by the template fitting, and its inferred stellar mass, which under CSFH scales with the assumed age, inherits this degeneracy, spanning $\log(M_\star/M_\odot) \simeq 9.5$–$9.9$ across the acceptable region. In Sect. 4.2.1, we attempt to constrain the M_{up} with He II-based diagnostics.

The $E(B-V)$ values from the BPASS+VMS fits are consistent with those from BPASS-only, as expected since they are constrained mainly by the continuum slopes β (Table 1). These values should be treated as upper limits on the stellar attenuation: we do not include a separate nebular-continuum component, which is not negligible at the young ages found here and is especially relevant for galaxies hosting VMS (Schaerer et al. 2025). The dust properties of both sources remain uncertain. In Sect. 3.3 we report a dust-continuum detection in J1429−0104 whose peak is offset by ~ 5 kpc from the rest-UV core, and the effective attenuation of the UV-emitting regions in both galaxies will require further investigation.

In summary, the template fitting shows that the rest-frame UV spectra of J1450−0144 and J1429−0104, and in particular their broad He II emission, are reproduced by the BPASS+VMS models but not by the BPASS-only models, indicating that both galaxies host substantial VMS populations. In Sect. 4.2 we further characterise the VMS populations more directly, comparing the measured equivalent widths of the wind lines with the model predictions to constrain M_{up} and to estimate the number of VMS in each galaxy. We also briefly discuss the broader implications of the VMS interpretation, for the high-mass end of the IMF, the chemical enrichment, and the eventual fate of these systems.

3.3 Molecular gas and dust

The ALMA observations provide a view of the cold ISM in these two galaxies, complementing the rest-frame UV information described above. Fig. 9 presents matched postage stamps (6.9″ × 6.9″) of J1450−0144 and J1429−0104, combining JWST/NIRSpec WATA images, Subaru/HSC (z- and y-band) imaging, and ALMA band-6 continuum and [C II] moment-0 maps. The measured [C II] fluxes and continuum flux densities are listed in Table 4, and the extracted [C II] spectra are shown in Fig. 8. Details of the continuum and moment-0 map construction, aperture choices, and flux extraction are given in Appendix A.

Both galaxies show clear detections of [C II] emission, but with different morphologies: J1429−0104 is marginally resolved, while J1450−0144 shows an unresolved core with a tentative extended component to the east. J1429−0104 also exhibits a significant dust continuum detection, whereas no continuum emission is detected for J1450−0144 at the current sensitivity. J1429−0104 additionally shows a clear spatial offset between its rest-frame UV emission and the [C II]/dust-continuum peaks, with the UV centroid displaced by $\sim 1''$ (~ 5.4 kpc at its redshift). We discuss the possible origin of this offset in Sect. 4.1.

The dust continuum detection in J1429−0104 allows us to derive the obscured star-formation rate and dust mass by fitting the observed flux density with a modified blackbody with $T_{dust} = 47$ K, $\beta = 1.6$, and $\kappa_\nu = 0.77\,(\nu/352\,\mathrm{GHz})^\beta\,\mathrm{cm^2\,g^{-1}}$ (Beelen et al. 2006; Decarli et al. 2018). We obtain $L_{TIR} = (2.6 \pm 0.4) \times 10^{12}\,L_\odot$ and

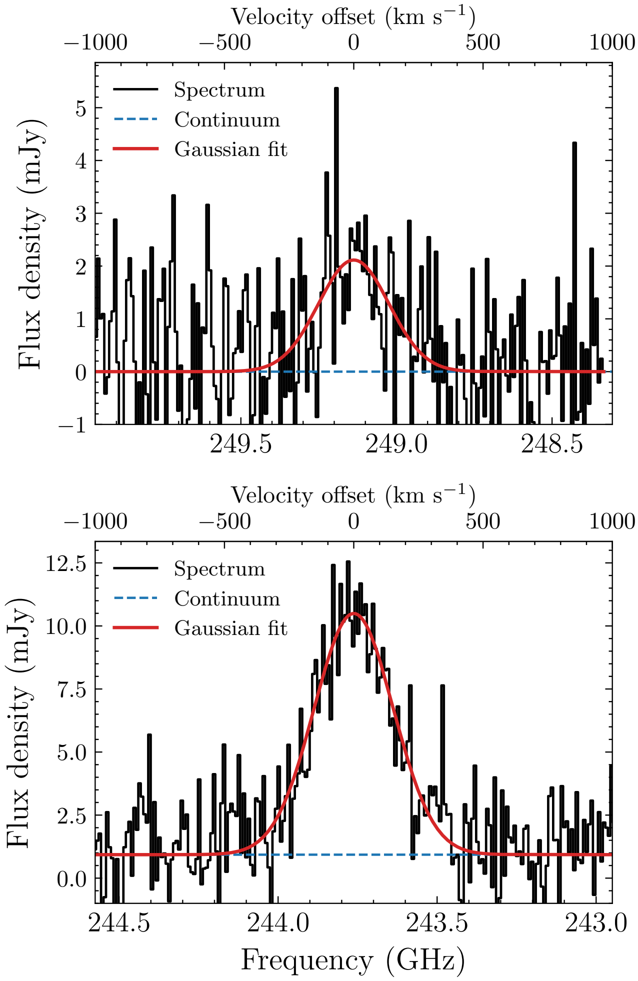

Figure 8. ALMA [C II] 158 μm spectra of J1450−0144 (top) and J1429−0104 (bottom), with the best-fit single-Gaussian model. The blue dashed line indicates the fitted continuum level. The upper axis shows the velocity offset relative to the systemic [C II] redshift of each source.

$M_{dust} = (1.2 \pm 0.2) \times 10^8\,M_\odot$, corresponding to an obscured star-formation rate $\mathrm{SFR_{IR}} = 310 \pm 50\,M_\odot\,\mathrm{yr^{-1}}$ following Inami et al. (2022). For J1450−0144, the continuum is not detected at the current sensitivity. We also estimate the molecular gas mass using the [C II]-based calibration of Zanella et al. (2018), $M_{mol} = \alpha_{[CII]}\,L_{[CII]}$ with $\alpha_{[CII]} = 30\,M_\odot/L_\odot$, yielding $M_{mol} = (1.24 \pm 0.07) \times 10^{11}\,M_\odot$ for J1429−0104 and $(0.24 \pm 0.05) \times 10^{11}\,M_\odot$ for J1450−0144. This calibration was derived from a sample of main-sequence and starbursting galaxies from $z \sim 0$ to $z \sim 6$ and carries an intrinsic scatter of ~ 0.3 dex. Its applicability to EUVLGs is untested, and the much harder and stronger radiation fields of EUVLGs may bias the calibration in either direction. All the measured and derived quantities are listed in Table 4. From a two-dimensional Gaussian fit to the [C II] moment-0 maps, J1429−0104 is resolved with a beam-deconvolved major-axis FWHM of $1.27 \pm 0.32''$ (6.8 ± 1.7 kpc), whereas J1450−0144's bright core is consistent being unresolved. Assuming the [C II] emission traces a rotating disc of diameter $D = 1.5\,a_{maj}$, the dynamical mass is $M_{dyn}\,\sin^2 i = 1.16 \times 10^5\,(0.75\,\mathrm{FWHM_{[CII]}}/\mathrm{km\,s^{-1}})^2\,(D/\mathrm{kpc})\,\mathrm{M_\odot}$ (Decarli et al. 2018), yielding $M_{dyn}\,\sin^2 i = (8.6 \pm 2.3) \times 10^{10}\,\mathrm{M_\odot}$ for J1429−0104 and, for the unresolved J1450−0144, an upper limit of $M_{dyn}\,\sin^2 i \lesssim 5 \times 10^{10}\,\mathrm{M_\odot}$ for any deconvolved size below the syn-

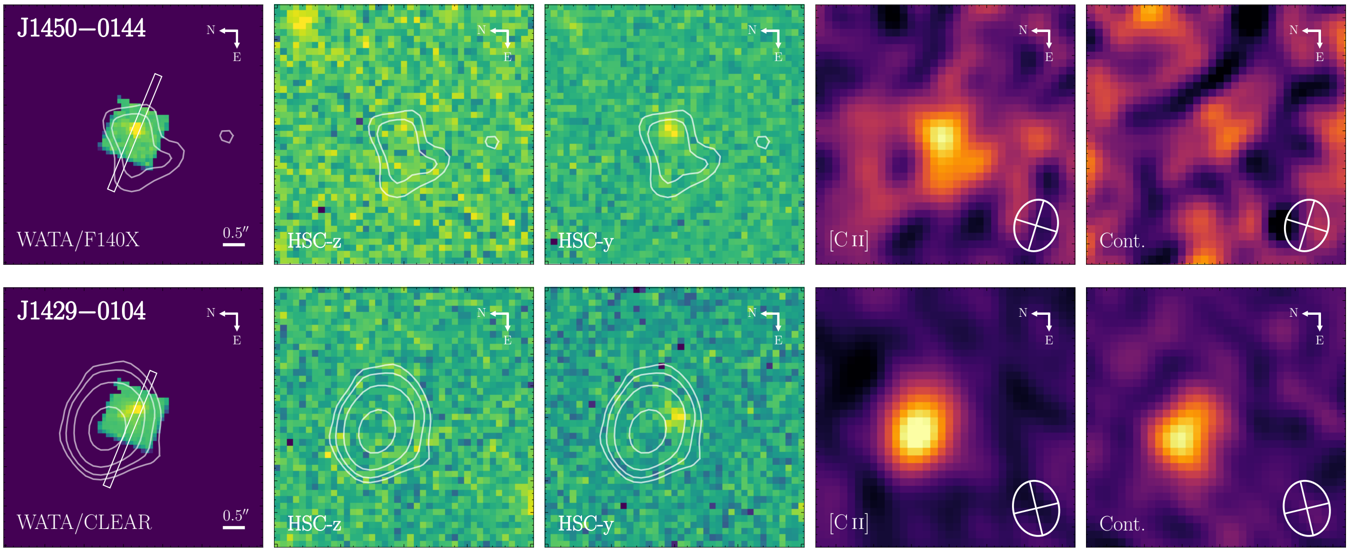

Figure 9. Multi-wavelength imaging of J1450−0144 (top row) and J1429−0104 (bottom row), each panel has a size of $6.9'' \times 6.9''$ and is oriented with north up and east left. From left to right: `JWST/NIRSpec` WATA acquisition image (F140X filter for J1450−0144, CLEAR for J1429−0104), Subaru/HSC z-band, y-band, ALMA band-6 [C II] 158 μm moment-0 map, and ALMA band-6 dust continuum map. White contours show the [C II] emission at 2, 3, 5, 10 σ, overlaid on the WATA, HSC z, and HSC y panels. The NIRSpec slit position is indicated on the WATA panels. ALMA synthesised beams are shown in the lower right of the ALMA panels. J1429−0104 shows a clear $\sim 1''$ (~ 5.4 kpc) offset between the rest-frame UV emission and the [C II]/dust-continuum peaks; in J1450−0144 the [C II] emission is approximately co-spatial with the UV centroid, and no continuum is detected at the current sensitivity.

thesised beam. For J1429−0104 the dynamical mass is comparable to $M_{\rm mol}$. For J1450−0144 the molecular gas mass is consistent with the dynamical limit. Together, these measurements place J1450−0144 and J1429−0104 among the most [C II]- and FIR-luminous galaxies known at $z > 6.5$. We discuss the broader implications of their IR properties in Sect. 4.1.

3.4 Lower limit of the number density of EUVLGs at cosmic dawn

The reclassification of J1429−0104 and J1450−0144 from quasars to star-forming galaxies raises a natural question: how common are such extreme UV-luminous galaxies during the epoch of reionisation?

Because both sources were originally included in the SHELLQs quasar sample, the survey volume and selection function needed to estimate their number density are already in place. Matsuoka et al. (2023) measured the quasar luminosity function at $z \sim 7$ with 35 spectroscopically confirmed objects over the $\sim$670 deg^2 of the HSC-SSP footprint available at the time of that study. With our revised UV magnitudes (Sect. 3.1; Table 1), both sources fall at $M_{1450} \approx -23.5$, and we therefore merge the two adjacent bins in the Matsuoka et al. (2023) luminosity function that originally contained them. Of the six sources in these merged bins, two are the EUVLGs presented here. Taking the mean luminosity function of the merged bin and scaling by the EUVLG fraction (2/6), we obtain a lower limit of $\Phi_{\rm EUVLG} \gtrsim 0.28\,{\rm Gpc^{-3}\,mag^{-1}}$ at $M_{1450} \approx -23.5$ and $z \sim 7$ (Fig. 10). This should be regarded as a lower limit because: First, the SHELLQs selection targets quasar-like colours and prominent Lyα emission; EUVLGs with weaker Lyα, different colors, or morphologies that fail the point-source criterion would not enter the sample. Second, only these two sources have been reclassified to date; additional SHELLQs objects at comparable luminosities and redshifts may likewise prove to be EUVLGs once NIR spectroscopy becomes available.

In Fig. 10 we also plot the galaxy UVLF at $z \sim 7$ from Bouwens et al. (2021) (Schechter function) and Harikane et al. (2025) (DPL). At $M_{1450} = -23.5$, these predict galaxy number densities of $\sim 3 \times 10^{-9}$ and $\sim 3 \times 10^{-8}\,{\rm Mpc^{-3}\,mag^{-1}}$, respectively. Comparing our EUVLG lower limit to these values implies a fraction of $\sim$1–10%. However, the bright end of the $z \sim 7$ galaxy UVLF remains loosely

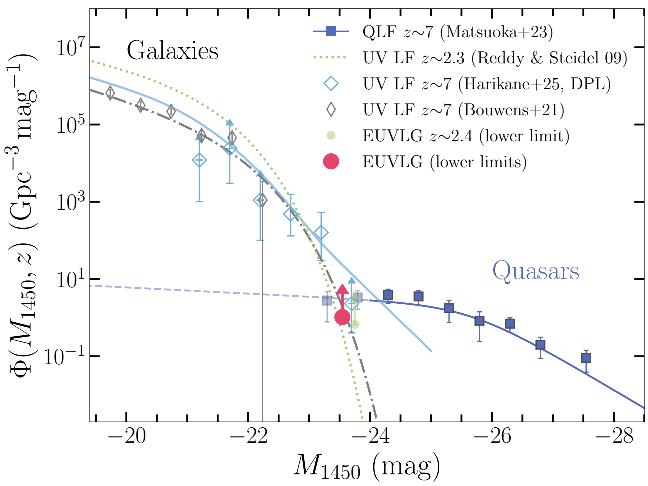

Figure 10. Lower limit on the EUVLG number density at $M_{1450} \approx -23.5$ and $z \sim 7$ (red), derived from the SHELLQs selection volume (Sect. 3.4), compared with the $z \sim 7$ quasar luminosity function (QLF; Matsuoka et al. 2023) and the $z \sim 7$ galaxy UV luminosity functions of Bouwens et al. (2021) (Schechter) and Harikane et al. (2025) (DPL). Green points and curves show the cosmic-noon comparison: the $z \sim 2.3$ star-forming galaxy UVLF of Reddy & Steidel (2009) (dotted), and a lower limit on the EUVLG number density at $z \sim 2.4$ (circle), obtained by integrating the eBOSS EUVLG sample over $-24.5 < M_{1450} < -23$ at $2 < z < 4$ (Upadhyaya et al. 2024; Dessauges-Zavadsky et al. 2025).

Table 4. ALMA-derived properties of J1450−0144 and J1429−0104. For J1450−0144, [C II] flux and luminosity are measured at the peak of the emission given its unresolved morphology. For J1429−0104, values are integrated within an elliptical aperture enclosing 90% of the curve-of-growth flux (Sect. 3.3). $L_{\rm FIR}$ (rest-frame 42.5–122.5 μm), $L_{\rm TIR}$ (rest-frame 8–1000 μm), and $M_{\rm dust}$ are derived from the measured continuum flux density assuming an optically thin modified blackbody with $T_{\rm dust}$ = 47 K and β = 1.6, following Beelen et al. (2006) and Decarli et al. (2018). $\rm SFR_{IR}$ is computed as $\rm SFR_{IR}/(M_\odot\,yr^{-1}) = 1.2 \times 10^{-10}\,L_{TIR}/L_\odot$ following Inami et al. (2022). $M_{\rm mol}$ is estimated from $L_{\rm [CII]}$ with a conversion factor $\alpha_{\rm [CII]} = 30\,M_\odot/L_\odot$ (Zanella et al. 2018). Quoted uncertainties are statistical only. Several derived quantities carry substantial additional systematics, most notably the $\sim$ 0.3 dex scatter in the $L_{\rm [CII]}$–$M_{\rm mol}$ relation and the unverified applicability of this calibration to UV-luminous sources at high redshift.

$F_{\rm [CII]}$ (Jy km s^{-1})	FWHM$_{\rm [CII]}$ (km s^{-1})	$L_{\rm [CII]}$ ($10^9\,L_\odot$)	$S_{\nu,\rm cont}$ (mJy)	$L_{\rm FIR}$ ($10^{12}\,L_\odot$)	$L_{\rm TIR}$ ($10^{12}\,L_\odot$)	$\rm SFR_{IR}$ ($M_\odot$ yr^{-1})	$M_{\rm dust}$ ($10^8\,M_\odot$)	$M_{\rm mol}$ ($10^{11}\,M_\odot$)
				J1450−0144				
0.72 ± 0.17	322 ± 56	0.79 ± 0.18	0.04 ± 0.05	0.06 ± 0.09	0.09 ± 0.13	10.99 ± 15.14	0.04 ± 0.06	0.24 ± 0.05
				J1429−0104				
3.67 ± 0.22	360 ± 16	4.14 ± 0.24	0.95 ± 0.14	1.84 ± 0.27	2.59 ± 0.39	311.40 ± 46.29	1.18 ± 0.17	1.24 ± 0.07

constrained. In Harikane et al. (2025) only four galaxies with $M_{\rm UV} < -23$ at $z \sim 7$, and in their brightest bin, $-24.5 < M_{\rm UV} < -23.5$, the number density is only a lower limit, based on a single data point. Robustly quantifying the EUVLG fraction at $z \sim 7$ therefore awaits larger spectroscopic samples at these luminosities. Nonetheless, the EUVLG phase is likely short-lived if the UV light is boosted by the massive stars, and its appearance in even this small sample raises the possibility that such episodes are common among UV-luminous galaxies during reionisation. At the same time, the faint end of the $z \sim 7$ quasar luminosity function (Matsuoka et al. 2023) should be revisited as more candidates receive spectroscopic follow-up. We also note that the GO 9180 target selection is biased towards SHELLQs sources with existing ALMA observations (Sect. 2.2). This restricts which sources could have been identified as EUVLGs, but does not affect the lower limit itself.

Finally, the green points and dotted curve in Fig. 10 place the cosmic-noon EUVLG population in context, alongside the $z \sim 2.3$ star-forming galaxy UV luminosity function of Reddy & Steidel (2009). The EUVLG number density is derived from the $\sim$ 70 EUVLGs identified at $2 < z < 4$ with $-24.5 < M_{\rm UV} < -23$ over the $\sim$ 9000 deg^2 eBOSS/SDSS footprint (Upadhyaya et al. 2024; Dessauges-Zavadsky et al. 2025, Marques-Chaves et al., in prep.), corresponding to a comoving number density of $\sim 10^{-9}$ Mpc^{-3}, or $\Phi_{\rm EUVLG} \sim 0.7$ Gpc^{-3} mag^{-1} when divided by the 1.5 mag width of the selection. The cosmic-noon EUVLGs lie well above the extrapolated bright end of the field-galaxy UVLF. However, it is too early to draw conclusions about the EUVLG fraction at either epoch or its evolution with redshift, since the bright end of the UVLF at $M_{\rm UV} < -23$ is poorly constrained at both cosmic noon and cosmic dawn. Both densities are also best regarded as lower limits, and pinning them down will require a systematic search for this population at both epochs.

4 DISCUSSION

4.1 A combined ultraviolet and far-infrared view

How do these two galaxies compare to other UV- or [C II]-luminous systems at the same epoch? In Fig. 11, we compare them with the REBELS sample at $z \sim 7$ (Bouwens et al. 2022; Inami et al. 2022) on the M_{1450}–$L_{\rm FIR}$ and M_{1450}–$L_{\rm [CII]}$ planes. We also show the unobscured star-formation rate $\rm SFR_{UV}$ converted from M_{1450} on the right axis, using the $\kappa_{\rm UV}$ factor from Upadhyaya et al. (2024) (see Sect. 3.1); the upper axes give the molecular gas mass $M_{\rm mol}$ converted from $L_{\rm [CII]}$ using $\alpha_{\rm [CII]}$ (Zanella et al. 2018), and the obscured star-formation rate $\rm SFR_{IR}$ converted from $L_{\rm FIR}$ through the $L_{\rm TIR}$ (Inami et al. 2022), both as described in Sect. 3.3. We also overplot the $z \sim 6$ quasar hosts of Decarli et al. (2018) and Izumi et al. (2021), as these are among the most [C II]-luminous and dust-rich systems known at these redshifts. Both of our galaxies are $\gtrsim$ 1 mag brighter in the rest-frame UV than typical REBELS galaxies, yet match the most FIR-luminous REBELS sources in [C II] and, for J1429−0104, in dust continuum. This places them among the most [C II]-luminous galaxies known at $z > 6.5$, with [C II] luminosities approaching those of luminous quasar hosts. J1429−0104, with $L_{\rm FIR} = 1.8 \times 10^{12}\,L_\odot$, sits firmly in the ultra-luminous infrared regime, and its obscured-to-total star-formation fraction $\rm SFR_{IR}/(SFR_{IR} + SFR_{UV}) \approx 70\%$ is in line with the high obscured fractions seen in the dustiest REBELS sources (Inami et al. 2022). The implied depletion time $\tau_{\rm dep} = M_{\rm mol}/{\rm SFR_{tot}} \sim 300$ Myr is comparable to that of main-sequence galaxies at similar redshifts, suggesting that the present burst can be sustained over a star-formation timescale provided the cold gas reservoir is not disrupted. We note, however, that both $M_{\rm mol}$ and $\rm SFR_{tot}$ are subject to substantial systematic uncertainties, and these numbers should therefore be taken as order-of-magnitude estimates.

The picture for J1450−0144 is qualitatively different: a clear [C II] detection but no dust-continuum signal, and a molecular gas reservoir (inferred from [C II]) several times smaller. At face value, J1450−0144 is at an earlier stage of the same process, consistent with the younger stellar population age inferred in Sect. 3.2. But whether the two galaxies represent successive snapshots of the same evolutionary track, or whether J1450−0144 has simply converted a smaller fraction of its cold ISM into obscured star formation cannot be settled with the present data. This will be an open question for ALMA follow-up of a larger EUVLG sample during reionisation.

Fig. 12 further illustrates this contrast in the IRX–β plane, comparing the infrared excess $\rm IRX = L_{TIR}/L_{UV,1600}$ with the observed UV continuum slopes (Sect. 3.1.1). J1450−0144 is undetected in the dust continuum, and its 2σ IRX upper limit is consistent with the canonical relations and with little obscured star formation. J1429−0104, by contrast, lies well above both the Calzetti-like and SMC-like relations even for $\beta_0 = -2.5$. A potential explanation is that the UV and FIR emission of J1429−0104 arises from spatially distinct regions, consistent with the $\sim$ 5.4 kpc offset between its rest-frame UV centroid and its [C II]/dust-continuum peak (Sect. 3.3). Comparable UV–FIR offsets have been reported in a subset of UV-bright galaxies at similar epochs: several REBELS sources show offsets of $\sim$ 0.5–1.5″

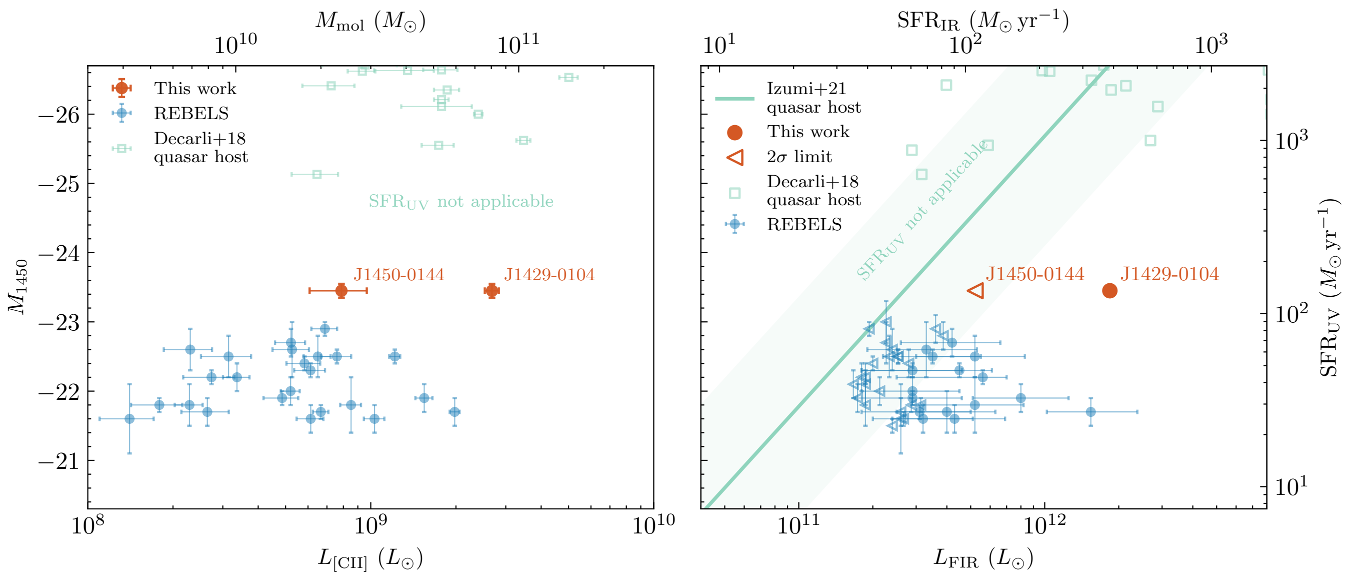

Figure 11. Rest-frame UV luminosity M_{1450} against [C II] 158 μm luminosity (left) and far-infrared luminosity (right) for the two galaxies presented in this work (red) and the REBELS sample at $z \sim 7$ (blue; Bouwens et al. 2022; Inami et al. 2022). *Left:* $L_{\rm [C\,II]}$ on the lower axis, with $z \gtrsim 6$ quasars for comparison (light green; Decarli et al. 2018). The upper axis gives the molecular gas mass $M_{\rm mol}$ inferred from $L_{\rm [C\,II]}$ via the Zanella et al. (2018) calibration. We caution that this conversion carries substantial systematic uncertainty and is calibrated predominantly on lower-z, less extreme star-forming galaxies. *Right:* $L_{\rm FIR}$ (8–1000 μm) on the lower axis, with the quasar host locus of Izumi et al. (2021) for reference (light green). The upper and right axes give the obscured and unobscured star-formation rates SFR$_{\rm IR}$ and SFR$_{\rm UV}$ (see Sect. 3.3). The SFR$_{\rm UV}$ does not apply to the quasar comparison samples, whose UV emission is AGN-dominated. J1450−0144 is plotted as a 2σ upper limit on $L_{\rm FIR}$. Our galaxies occupy the extreme high-SFR regime in both unobscured and obscured star formation, appearing as a luminous extension of the REBELS population.

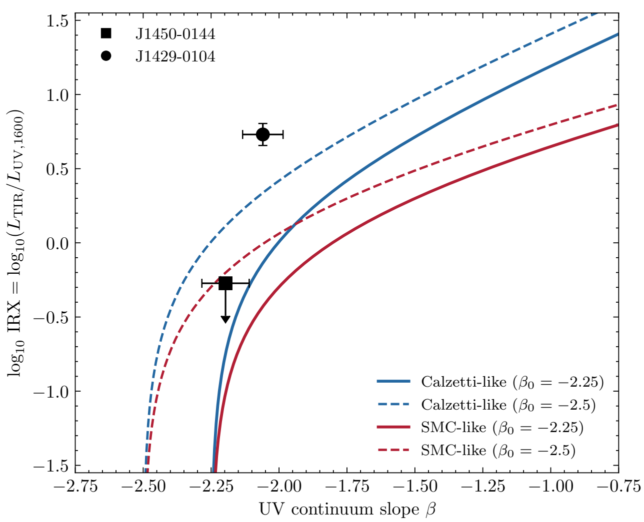

Figure 12. IRX–β diagram for J1450−0144 and J1429−0104. The infrared excess IRX = $L_{\rm TIR}/L_{\rm UV,1600}$ is computed from $L_{\rm TIR}$ in Table 4 and the rest-frame UV luminosity at rest-frame wavelength $\lambda_{\rm rest}$ = 1600. The UV continuum slopes β are measured in Sect. 3.1.1. J1429−0104 is detected in the dust continuum, while J1450−0144 is shown as a 2σ upper limit on IRX. Curves show the relations expected for Calzetti-like and SMC-like dust attenuation with $\beta_0 = -2.25$ and -2.5.

($\sim$ 3–8 kpc) between the rest-UV and dust peaks (Inami et al. 2022; Bowler et al. 2024), and roughly 30% of ALPINE main-sequence galaxies at $z \sim$ 4–6 display significant ($> 3\sigma$) offsets with a median of $\sim$ 3.5–4.5 kpc (Killi et al. 2024). Several physical scenarios are typically invoked: an ongoing merger between an unobscured and an obscured component; a single galaxy with an inhomogeneous dust distribution, in which a heavily obscured central region hides the true star-formation peak while the observed UV centroid traces a less-attenuated, off-centre clump (Bowler et al. 2024; Ocvirk et al. 2025); or radiation-pressure-driven outflows from the young stellar population that displace dust away from the UV-emitting region (Ferrara et al. 2023; Ziparo et al. 2023). With the present data we cannot distinguish between these scenarios. High-resolution imaging in the rest-frame UV/optical and IR, will be critical to determine whether the offset reflects a merger, an obscured central starburst, or feedback-driven dust displacement.

4.2 Very massive stars at reionisation: constraints and implications

4.2.1 *Constraining the upper-mass cutoff $M_{\rm up}$ of the initial mass function with UV wind diagnostics*

Sect. 3.2 established that reproducing the broad He II λ1640 emission requires models with dedicated very massive star wind physics. To constrain the VMS content more directly, we follow Upadhyaya et al. (2024) and compare the data with the `BPASS+VMS` grid in the He II–N V and He II–C IV equivalent-width planes. The three lines trace different parts of the massive-star population. N V and C IV are resonance lines of high-ionisation states. Even winds of modest density imprint P Cygni profiles on the photospheric continuum, while maintaining the high ionisation requires the hard radiation field of the hottest stars. They are therefore sensitive tracers of young massive stars in general, not necessarily the very massive ones, and their strengths decline as the population ages. He II is not a resonance line,

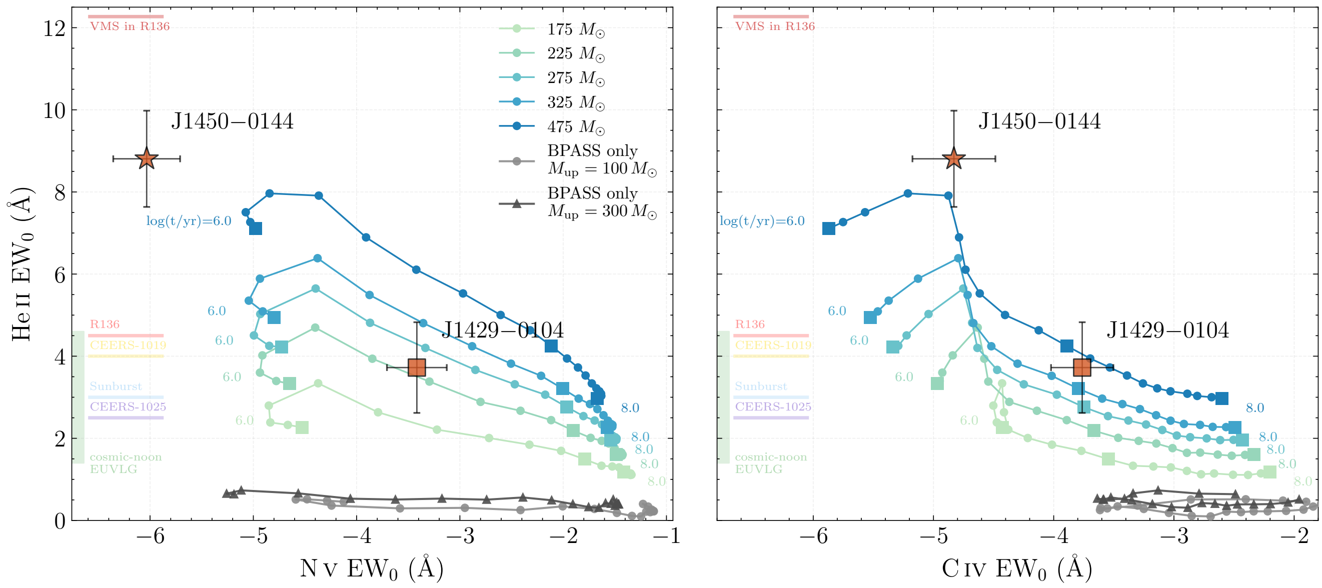

Figure 13. Diagnostic equivalent-width diagrams comparing the rest-frame UV wind features of J1450−0144 (star) and J1429−0104 (square) with `BPASS+VMS` population synthesis models from Upadhyaya et al. (2024), which incorporate VMS spectroscopic models from Martins & Palacios (2022). Left: He II λ1640 vs. N V λ1240 EW$_0$. Right: He II λ1640 vs. C IV λ1550 EW$_0$. Coloured tracks correspond to models at $Z = 0.006$ with a Salpeter IMF and upper-mass cutoffs $M_{\rm up} = 175$, 225, 275, 325, and 475 $M_\odot$ (light green to blue) with a constant star-formation. Filled circles along each track mark the evolution of the population from $\log(t/{\rm yr}) = 6.0$ to 8.0 in steps of $\Delta\log(t/{\rm yr}) = 0.1$, with the $\log(t/{\rm yr}) = 6.0$ starting point labelled on each track. For reference, grey tracks show standard BPASS models without the Martins & Palacios (2022) models for $M_{\rm up} = 100\,M_\odot$ (circles) and $M_{\rm up} = 300\,M_\odot$ (triangles). Coloured bands at the left of each panel mark the He II EW$_0$ of literature systems hosting confirmed or candidate VMS, placed along the He II axis only: The stacked spectrum of seven VMS in R136, the entire R136 cluster (Crowther et al. 2016), the $z \simeq 8.7$ galaxies CEERS-1019 and CEERS-1025 (Marques-Chaves et al. 2026), the Sunburst cluster (Meštrić et al. 2023; Welch et al. 2025), and the cosmic-noon EUVLG sample, whose vertical band spans the observed range (Upadhyaya et al. 2024). Both galaxies fall in the region of the diagram occupied by very young, VMS-rich populations.

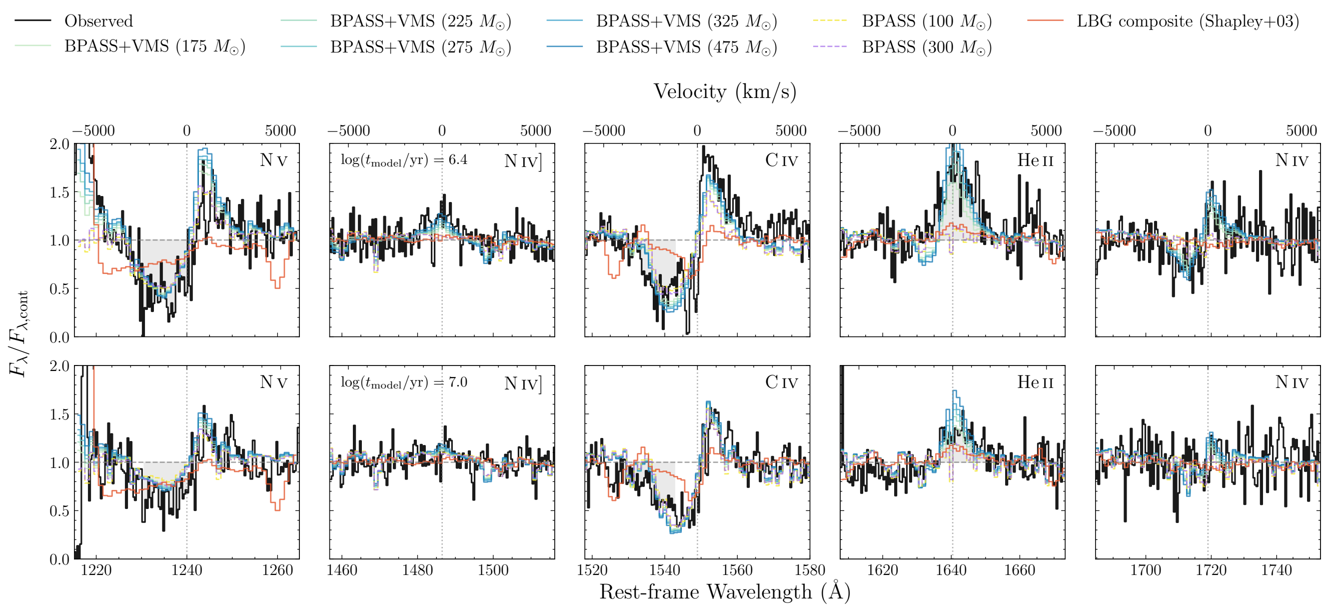

Figure 14. Comparison of the rest-frame UV spectra of J1450−0144 (top row) and J1429−0104 (bottom row) with BPASS population synthesis models including very massive stars, around the five key wind-line and emission diagnostics (left to right): N V λ1240, N IV] λ1486, C IV λ1550, He II λ1640, and N IV λ1719. Black curves show the observed spectra normalised by the local continuum. Coloured curves show BPASS+VMS models from Upadhyaya et al. (2024), which incorporate the VMS stellar evolution and atmosphere models of Martins & Palacios (2022), with IMF upper-mass limits $M_{\rm up} = 175$, 225, 275, 325, and 475 $M_\odot$ (light to dark blue), evaluated at the inferred ages of $\log(t/{\rm yr}) = 6.4$ for J1450−0144 and 7.0 for J1429−0104 based on the right panel of Fig. 13. Dashed curves show standard BPASS models without VMS treatment for $M_{\rm up} = 100$ (yellow) and 300 $M_\odot$ (violet). The orange curve is the composite LBG spectrum from Shapley et al. (2003), shown for reference. Vertical dotted lines mark the systemic wavelengths of each transition. The BPASS+VMS models reproduce the P Cygni profiles in N V and C IV and the broad He II λ1640 emission, while standard BPASS and the LBG composite fall well short. J1450−0144 also shows clear broad N IV] λ1486 and N IV λ1719 emission predicted by the VMS models; in J1429−0104, these features are weaker.

so it cannot form by scattering the stellar continuum. Instead it is produced by recombination in the wind itself, with an emissivity that scales as the square of the wind density (Gräfener 2021; Martins & Palacios 2022). In the models, only VMS near the Eddington limit sustain winds dense enough to power strong broad He II, so its equivalent width serves as a good tracer of the VMS population. Following Upadhyaya et al. (2024), the rest-frame equivalent widths are measured by direct integration over fixed windows in both the data and the synthetic spectra (He II over 1630–1655 Å, C IV over 1530–1543 Å, N V over 1230–1240 Å), using the spline continuum of Sect. 2.2.2 for the data and local sidebands for the models. Adopting local sidebands for the data instead would slightly raise the measured EW_0 of both sources, moving them further into the VMS regime.

Fig. 13 shows the comparison, with He II EW_0 plotted against N V EW_0 (left) and C IV EW_0 (right). Coloured tracks correspond to different upper-mass limits, from $M_{\rm up} = 175$ to $475\,M_\odot$, each evolving over $\log(t/{\rm yr}) = 6$–8. We also show the two `BPASS-only` tracks in grey as references. We can see that even extending the IMF to $M_{\rm up} = 300\,M_\odot$, the strength of the He II emission remains $\lesssim 1$ Å because their massive stars never develop the optically-thick winds. The measurements for the two galaxies are overplotted as a star (J1450−0144) and a square (J1429−0104). Coloured bands at the left of each panel mark the He II EW_0 of literature systems (star clusters and galaxies) hosting confirmed or candidate VMS, placed along the He II axis only: the R136 cluster and the seven VMS within it (Crowther et al. 2016), the $z \simeq 8.7$ galaxies CEERS-1019 and CEERS-1025 (Marques-Chaves et al. 2026), the Sunburst cluster (Meštrić et al. 2023; Welch et al. 2025), and the cosmic-noon EUVLG sample (Upadhyaya et al. 2024). As a complementary check on the line profiles, Fig. 14 overlays the same model grid, evaluated at the closest-matching ages in the He II versus C IV diagram for the two galaxies ($\log(t/{\rm yr}) = 6.4$ for J1450−0144 and 7.0 for J1429−0104), on the observed spectra around the five key wind diagnostics (N V, C IV, He II plus N IV] λ1486 and N IV λ1719).

We can clearly see that for J1450−0144, its extreme He II EW_0 with a very deep N V trough place it above the majority of the literature values and beyond the model grid in both panels. Only the composite of the seven VMS in R136 has a stronger but comparable He II. J1429−0104 lies further along the tracks, suggesting it being a more evolved system than J1450−0144, and its position in the He II–N V plane is consistent with the $M_{\rm up} = 225\,M_\odot$ track. The relative strengths of C IV and N V are, however, not fully consistent with the models for either galaxy: at the positions implied by He II and N V, the observed C IV troughs are shallower than predicted, so the He II–C IV plane favours somewhat older populations. As seen in Fig. 14, the observed C IV profiles show more complex structure than the models, and emission features superposed on the P-Cygni trough may bias the integrated EW_0 towards less negative values. Detailed modelling of this profile is deferred to future work.

One minor inconsistency is that the `BPASS+VMS` models generally predict a P Cygni profile for He II as well (see Fig. 14), which is not evident in our spectra (tentative in J1429−0104), plausibly because the stellar wind is not optically thick to this non-resonant transition. We confirmed that repeating the He II EW_0 measurements using only the red emission wing of the line for both the data and the models leaves the conclusions unchanged, i.e. both galaxies remain most consistent with $M_{\rm up} \gtrsim 225 - 475\,M_\odot$.

For J1450−0144, the diagnostic favours a higher upper-mass limit than the template fitting in Sect. 3.2 ($M_{\rm up} = 275\,M_\odot$). This is somewhat expected as the template fitting need to consider several P Cygni profiles, which respond only weakly to $M_{\rm up}$, whereas the diagnostic isolates the He II emission that traces the VMS content most directly. Fig. 14 indeed shows that, at these young ages, the models with the largest $M_{\rm up}$ provide a better match to the observed He II profiles. However, we note that these $M_{\rm up}$ constraints are strongly model dependent. The Gräfener (2021) mass-loss prescription underlying the grid is calibrated on the VMS in the LMC, and no empirical constraints on VMS winds exist at other metallicities. Martins et al. (2025) show that the predicted He II strength at fixed $M_{\rm up}$ changes drastically depending on whether or not VMS mass-loss rates scale with metallicity. In addition, the grid fixes the IMF slope at the Salpeter value. We therefore consider the presence of a substantial VMS population as robust, since no model without appropriate VMS wind physics approaches the observed He II strengths, while pinning down $M_{\rm up}$ and the detailed shape of the high-mass IMF will require VMS wind models calibrated beyond the LMC and deeper spectroscopy of larger samples.

4.2.2 *The number of very massive stars in these two galaxies*

Besides the upper-mass cutoff, another quantity of interest is the total number of VMS that these two galaxies host. For a galaxy with $10^9\,M_\odot$ solar masses formed in a burst with a Salpeter IMF extending to $M_{\rm up} = 300\,M_\odot$, direct integration of the IMF gives $N_{\rm VMS} \approx 2\times10^5$ stars above $100\,M_\odot$ at birth. Given the stellar masses of $\log(M_\star/M_\odot) \gtrsim 9$ and ages comparable to the VMS lifetime inferred in Sect. 3.2, both galaxies are thus expected to host of order $\gtrsim 10^5$ VMS at birth and a comparable number of living VMS.

We cross-check it based on the UV continuum luminosity. Martins & Palacios (2022) show that, in a young starburst with a Salpeter IMF extended to $300\,M_\odot$, stars with $M \gtrsim 100\,M_\odot$ contribute nearly as much UV light as the rest of the population combined (their Fig. 8), so that VMS account for $f_{\rm VMS} \sim 0.5$ of the integrated UV continuum. The depth of the C IV P Cygni troughs in our spectra supports a comparably large contribution from strong-wind stars. In the integrated spectrum, the trough is a luminosity-weighted average over stars with and without the wind feature. That is, if the absorption in the individual strong-wind stars is saturated, the residual flux at the trough bottom measures the fraction of the continuum contributed by stars without such winds. The observed troughs reach $F_\lambda/F_{\rm cont} \approx 0.2$–0.5 (Sect. 3.1.2), implying that $\sim$ 50–80 per cent of the UV continuum arises from stars with dense winds. Since ordinary early-O stars also contribute to the C IV absorption, and incomplete saturation or velocity-dependent overlap of the individual profiles would fill in the trough, this is an upper limit on $f_{\rm VMS}$, broadly consistent with $f_{\rm VMS} \sim 0.5$. The number of VMS is then $N_{\rm VMS} \approx f_{\rm VMS}\, L_{\lambda,{\rm UV}}/l^{\rm VMS}_{\lambda,{\rm UV}}$, where $l^{\rm VMS}_{\lambda,{\rm UV}} \sim 10^{36}$–$10^{37}$ erg s^{-1} Å^{-1} for individual VMS with $M \sim$ 150–400 $M_\odot$ (Martins & Palacios 2022). For $M_{\rm UV} = -23.5$ ($L_{\lambda,{\rm UV}} \approx 1.5\times10^{42}$ erg s^{-1} Å^{-1}), this yields $N_{\rm VMS} \sim 10^5$–10^6, in agreement with the fit-based estimate.

We could imagine that a VMS population of this size could significantly impact the entire galaxy. In the following sections, we discuss what these VMS imply for the high-mass end of the IMF (Sect. 4.2.3), how their winds may enrich the surrounding ISM (Sect. 4.2.4), and the potential large number of pair-instability supernovae and stellar-mass black holes they will leave behind (Sect. 4.2.5).

4.2.3 *Very massive star formation in EUVLGs and the initial mass function*

For decades the stellar upper mass limit was thought to be $\lesssim 150\,M_\odot$ (e.g. Figer 2005). This limit has since been revised upward, first by re-analyses of the WNh stars in R136 (Crowther et al. 2010, 2016) and the $\sim 200\,M_\odot$ stars in the Sunburst LyC cluster at $z = 2.37$ (Vanzella et al. 2022; Meštrić et al. 2023), and more recently by VMS signatures in cosmic-noon EUVLGs (Upadhyaya et al. 2024), in JWST-discovered high-z galaxies (Marques-Chaves et al. 2026; Chen et al. 2026), and in the two $z > 6$ EUVLGs presented in this work. The local VMS hosts are all young, dense star clusters with central densities $\rho_\star \gtrsim 10^4\,M_\odot\,\mathrm{pc}^{-3}$, consistent with theoretical expectations that VMS form in such environments via direct accretion, binary mergers, or runaway collisions (e.g. Portegies Zwart et al. 1999; Krumholz et al. 2009; Banerjee et al. 2012; Vink et al. 2015). The compact sizes, high gas surface densities, and low metallicities common at $z \gtrsim 6$ make the epoch of reionisation favourable for VMS formation.

Testing this picture for J1450−0144 and J1429−0104 requires knowing their internal structure. Reionisation-epoch galaxies observed with JWST are preferentially clumpy in the rest-frame UV, with ~ 150–250 pc clumps and star-forming complexes identified at $z \simeq 6$–8 (Chen et al. 2023; Zhu et al. 2026). Our current imaging resolves scales of only $\sim 0.1''$ (~ 0.5 kpc at these redshifts), a factor of ~ 2–3 too coarse to identify such clumps, let alone individual giant molecular clouds. Higher-resolution JWST/NIRCam imaging, or follow-up of strongly lensed analogues, will be needed to link these galaxies to the compact-cluster channel seen locally.

On the IMF side, the detection of a substantial VMS population does not, on its own, require a top-heavy IMF. A standard Salpeter or Kroupa IMF extended to $M_\mathrm{up} \sim 200$–$500\,M_\odot$ already yields $\gtrsim 10^5$ stars above $100\,M_\odot$ for a galaxy with $\log(M_\star/M_\odot) \sim 9$ (Sect. 4.2.2). The principal observational lever is therefore not the existence of VMS but the upper-mass cutoff M_up. At the same time, our constraints on M_up in Sect. 4.2.1 should be regarded as only indicative, since several physical inputs of current VMS models are not yet well understood (e.g. Gräfener 2021; Martins & Palacios 2022; Sabhahit et al. 2023; Schaerer et al. 2025).

Even so, if VMS are widespread at $z \gtrsim 6$, they dominate the integrated ionising-photon production, kinetic wind energy, and metal yields per unit stellar mass formed. Standard SFR and stellar-mass calibrations with IMF cutoffs of 100–$150\,M_\odot$ do not capture these contributions. If compact starbursts of the kind seen here are a common phase among UV-luminous reionisation-epoch galaxies, the high-mass IMF cutoff deserves systematic re-examination in observational calibrations and cosmological simulations.

4.2.4 Chemical yields and the connection to high-redshift N-emitters

JWST has revealed an unexpected population of high-redshift galaxies with log(N/O) above the solar value at sub-solar metallicity (e.g., Bunker et al. 2023; Cameron et al. 2023; Marques-Chaves et al. 2024; Schaerer et al. 2024; Ji et al. 2024; Topping et al. 2024; Berg et al. 2025), roughly an order of magnitude higher than the local N/O–O/H relation (Cataldi et al. 2025). The inferred stellar ages of many of these systems are far shorter than the $\gtrsim 30$ Myr needed for intermediate-mass AGB stars, the standard channel for primary nitrogen enrichment, to return their CNO-processed envelopes to the ISM (e.g., Cameron et al. 2023; Marques-Chaves et al. 2024).

A more rapid alternative is the direct release of CNO-cycle H-burning products through massive-star winds during main-sequence evolution. Proposed polluters operating on Myr timescales include classical Wolf–Rayet stars (e.g., Isobe et al. 2023), VMS (Vink 2023; Shi et al. 2026; Cameron et al. 2026), and hypothetical supermassive stars (SMS; $M \sim 10^3$–$10^4\,M_\odot$; Charbonnel et al. 2023). Vink (2023) argued that VMS are a particularly promising channel. They are observationally established from the local universe to the epoch of reionisation (Marques-Chaves et al. 2026, and this work). Their large convective cores and proximity to the Eddington limit enrich their surfaces in N already on the main sequence, while N is being synthesised rather than destroyed. Their dense, optically thick winds then eject this material at terminal velocities well below those of cWR stars, which favours retention within the host star-forming region.

In J1450−0144 we detect clear broad N iv] $\lambda1486$ emission together with a prominent N iv $\lambda1719$ P Cygni feature, while in J1429−0104 the N iv] detection is only marginal (Fig. 14). These are likely stellar wind signatures arising in the dense, accelerating outflows of WNh-type VMS (Martins & Palacios 2022), and they probe the surface and wind composition of the stars rather than the ambient ISM. The N iii] $\lambda1750$ line, the typical nebular signature of JWST-discovered N-emitters, is not detected in our spectra, while C iii] $\lambda1909$ and O iii] $\lambda1666$ are detected (Table 2). The C iii] line is broad, however, with FWHM exceeding $1000\,\mathrm{km\,s^{-1}}$, which suggests a partial stellar-wind contribution. The absence of nebular nitrogen features alongside clear VMS wind signatures could indicate that the enriched material has not yet mixed into the ionised ISM, that the radiation field properties differ, or that the gas-phase abundance pattern genuinely differs from that of canonical N-emitters. We caution that the non-detection of a single line is not an abundance measurement. Either way, EUVLGs with clear stellar VMS signatures are ideal laboratories for testing how VMS yields are transferred into the surrounding ISM. A gas-phase N/O measurement would require deeper limits on nebular N iv] and N iii] $\lambda1750$ relative to O iii] $\lambda1666$, anchored by rest-frame optical [O iii] and Hβ to constrain the oxygen abundance and reddening.

4.2.5 The endpoint of an EUVLG phase

VMS lifetimes are short ($\lesssim 3$ Myr; e.g., Yusof et al. 2013; Vink et al. 2015; Costa et al. 2025), so at the ages derived in Sect. 3.2 many members of the VMS population must already be reaching the end of their evolution. Their fates depend sensitively on the zero-age main-sequence mass (ZAMS) and on the uncertain wind mass-loss history (Woosley & Heger 2015; Vink 2015). At SMC-like metallicity (Yusof et al. 2013), stars of ~ 70–$100\,M_\odot$ undergo pulsational pair-instability supernovae, which eject the outer layers in a series of thermonuclear pulses but leave $\sim 40\,M_\odot$ black holes. Stars of ~ 100–$290\,M_\odot$ are fully disrupted as pair-instability supernovae (PISNe) and leave no remnant. Above $\sim 290\,M_\odot$, the star collapses directly to a black hole with little or no mass ejection. These boundaries are sensitive to mass loss, rotation, and convective overshooting, and vary substantially between stellar-evolution codes (Woosley & Heger 2015). For the $N_\mathrm{VMS} \sim 10^5$–10^6 estimated for the two galaxies (Sect. 4.2.2), the implied PISN rate is of order 10^{-3}–$10^{-2}\,\mathrm{yr}^{-1}$ per galaxy, depending on the exact star-formation history.

A potentially more important question is the collective fate of the host clusters themselves. The stars that evade the PISN channel will leave behind a large population of black hole remnants, from the $\sim 40\,M_\odot$ PPISN products to the considerably more massive remnants of direct collapse, concentrated in the compact star-forming cores. Whether these remnants can grow significantly by accreting the leftover in-situ gas is unclear. Idealised simulations of compact GMCs by Shi & Murray (2026), with initial cloud masses up to $\sim 10^9\,M_\odot$ within ~ 500 pc (broadly comparable to the stellar masses and compact morphologies of our two sources), suggest that stellar feedback typically expels the surrounding gas before significant accretion onto the remnants can occur, so individual black holes remain at $\lesssim 500\,M_\odot$

within the first ~ 10 Myr. Even this bound is reached only in their most extended, lowest-metallicity ($Z = 0.01\,Z_\odot$) configuration. At the $Z \sim 0.2\,Z_\odot$ inferred for our galaxies, stronger winds and earlier gas expulsion are thought to suppress in-situ growth even further. These results also rest on a limited set of cloud configurations and sub-grid prescriptions, and do not follow the long-term post-starburst evolution. A complementary dynamical channel bypasses this bottleneck. In sufficiently dense young clusters, runaway main-sequence stellar collisions have been proposed to assemble a single supermassive object that collapses into an intermediate-mass black hole (IMBH) seed of $\sim 10^3\,M_\odot$ (e.g., Portegies Zwart et al. 2004; Gürkan et al. 2004; Shi et al. 2021). Repeated tidal disruptions, BH–BH mergers, and hierarchical cluster mergers could in principle grow these seeds further (e.g., Rantala et al. 2024). Whether any of these pathways can bridge the gap to the $\sim 10^8$–$10^9\,M_\odot$ SMBHs observed in luminous $z \sim 6$–7 quasars (Fan et al. 2023) remains an open question (Inayoshi et al. 2020; Volonteri et al. 2021). These high-redshift EUVLGs, which combine large VMS populations, compact star-forming structures, and relatively low metallicities, could nonetheless provide distinctive hints for discriminating between these seeding and growth scenarios.

5 CONCLUSIONS

We have presented JWST/NIRSpec and ALMA Band-6 observations of two SHELLQs sources at $z > 6.5$, J1450−0144 ($z = 6.63$) and J1429−0104 ($z = 6.80$), originally classified as faint quasars on the basis of their quasar-like UV luminosities ($M_{\rm UV} \approx -23.5$), strong Lyα emission and blue UV continua (Matsuoka et al. 2018a, 2022). The new spectroscopy overturns this classification and yields a consistent physical picture of both sources. We summarise our key findings below.

1. ***Two "high-z quasars" reclassified as EUVLGs at the epoch of reionisation.*** The rest-frame UV spectra of both sources exhibit blue continua, prominent P Cygni profiles in N v λ1240, Si iv λ1400, and C iv λ1550, broad He ii λ1640 emission, and narrow nebular lines including [O ii] $\lambda\lambda$3727, 3730 and [Ne iii] $\lambda\lambda$3870, 3969. Neither source shows broad Lyα or Mg ii $\lambda\lambda$2796, 2804 emission. These properties are inconsistent with a type-I quasar interpretation. Instead, both spectra closely match the cosmic-noon EUVLG population (Marques-Chaves et al. 2020, 2021, 2022; Upadhyaya et al. 2024) and resemble the stacked spectrum of the seven most massive stars in the R136 cluster (Crowther et al. 2016). J1450−0144 and J1429−0104 are therefore the first spectroscopically confirmed EUVLGs at $z > 6.5$ with $M_{\rm UV}$ brighter than −23 (Sect. 3.1).
2. ***Young, intensely star-forming stellar populations with very massive stars.*** We fit the continuum-normalised N v, C iv, and He ii wind profiles of both galaxies with `BPASS-only` and `BPASS+VMS` models at $Z = 0.006$ under a constant star-formation history. The `BPASS-only` models reproduce the N v and C iv P Cygni profiles but underpredict the broad He ii emission (FWHM $\simeq$ 1900 and 2200 km s^{-1}, EW$_0$ = 8.8 ± 1.2 and 3.7 ± 1.1 Å, for J1450−0144 and J1429−0104, respectively), whereas the `BPASS+VMS` models reproduce all three features, and the dedicated VMS wind physics of Martins & Palacios (2022) may be the key ingredient. The best-fit `BPASS+VMS` templates additionally predict broad N iv] λ1486 emission and a N iv λ1719 P Cygni profile, two further characteristic VMS signatures. Both are clearly detected in J1450−0144, while in J1429−0104 the N iv] emission is only marginal. Under the `BPASS+VMS` models, J1450−0144 hosts a tightly constrained, very young population, with a star-formation duration of 2–4 Myr and $\log(M_\star/M_\odot) \approx 9.2$. For J1429−0104 the duration and $M_{\rm up}$ are degenerate: only the combination of ages $\lesssim 3$ Myr and $M_{\rm up} \gtrsim 325\,M_\odot$ is excluded, and the inferred stellar mass spans $\log(M_\star/M_\odot) \approx 9.5$–9.9 across the acceptable region. Scaling the best-fit templates to the observed flux implies star-formation rates of SFR $\simeq$ 540 and $\simeq 300\,M_\odot\,{\rm yr}^{-1}$ for J1450−0144 and J1429−0104, respectively (Sect. 3.2).
3. ***Massive cold gas reservoirs and contrasting obscured star formation.*** ALMA reveals luminous [C ii] 158 μm emission in both sources ($L_{\rm [CII]} \simeq 0.8$ and $4.1 \times 10^9\,L_\odot$ for J1450−0144 and J1429−0104, respectively) and a clear dust-continuum detection in J1429−0104 ($L_{\rm TIR} \simeq 2.6 \times 10^{12}\,L_\odot$, SFR$_{\rm IR} \simeq 310\,M_\odot\,{\rm yr}^{-1}$), while J1450−0144 remains undetected in the continuum. Both galaxies are $\gtrsim$ 1 mag brighter in the rest-frame UV than typical REBELS galaxies yet match the most [C ii]-luminous REBELS sources, and the implied molecular gas masses of $M_{\rm mol} \sim 10^{10}$–$10^{11}\,M_\odot$ correspond to depletion times of a few hundred Myr, sufficient to sustain the present star-formation episodes provided the gas reservoirs are not disrupted. The two galaxies nonetheless differ sharply in obscuration: J1429−0104 sits in the ultra-luminous infrared regime with an obscured-to-total star-formation fraction of $\approx$ 70 per cent and lies well above the Calzetti-like and SMC-like IRX–β relations, whereas the 2σ IRX upper limit of J1450−0144 is consistent with little obscured star formation. A potential explanation for the IRX excess of J1429−0104 is that its UV and FIR emission arise from spatially distinct regions, consistent with the $\sim 1''$ ($\sim$ 5.4 kpc) offset between its rest-UV centroid and the [C ii]/dust peak, whose origin (a merger, an obscured central starburst, or feedback-driven dust displacement) require future high-resolution imaging (Sect. 3.3 and 4.1).
4. ***EUVLGs are not vanishingly rare during reionisation.*** Using the SHELLQs selection volume, we derive a lower limit on the EUVLG number density of $\Phi_{\rm EUVLG} \gtrsim 0.28\,{\rm Gpc}^{-3}\,{\rm mag}^{-1}$ at $M_{1450} \approx -23.5$ and $z \sim 7$. Compared with the $z \sim 7$ galaxy UVLFs, this corresponds to an occupation fraction of $\gtrsim$ 1–10 per cent for the EUVLG phase among UV-luminous galaxies at this magnitude, itself a lower limit given the quasar-oriented SHELLQs selection. Robust quantification awaits larger spectroscopic samples at these luminosities (Sect. 3.4).
5. ***Constraints on the upper-mass cutoff and the size of the VMS population.*** In the He ii–N v and He ii–C iv equivalent-width planes, J1429−0104 is consistent with `BPASS+VMS` models with $M_{\rm up} \gtrsim 225\,M_\odot$, while J1450−0144 lies beyond even our most extreme grid, implying $M_{\rm up} \gtrsim 475\,M_\odot$. We note that these cutoffs are strongly model dependent, but the presence of a substantial VMS population is robust. The depth of the C iv P Cygni troughs implies that $\sim$ 50–80 per cent of the UV continuum arises from stars with dense winds, an upper limit on the VMS contribution broadly consistent with the $f_{\rm VMS} \sim 0.5$ expected for a young population with a Salpeter IMF extending to 300 $M_\odot$. Both direct IMF integration and the UV luminosity budget imply $N_{\rm VMS} \sim 10^5$–10^6 in each galaxy (Sect. 4.2.1 and 4.2.2).

Taken together, these results identify J1450−0144 and J1429−0104 as a new class of laboratory at the very bright end of the UVLF at high redshift: compact, gas-rich, intensely star-forming galaxies that simultaneously host substantial very massive star populations. They sit at the intersection of several open problems — the IMF in low-metallicity starbursts, the origin of the nitrogen enhancement at high redshift, the escape of ionising radiation from luminous starbursts, and perhaps the formation of supermassive black holes through dense-cluster pathways. None of these connections is resolved by the present data alone, but the existence of even two such systems in a small reclassified sample suggests that many more EUVLGs await identification in the wide-area surveys of the coming decade, including *Euclid* and the *Roman Space Telescope*, which together will begin to chart this population across the reionisation epoch.

ACKNOWLEDGEMENTS

D. Yang thanks the members of the ENIGMA group at UC Santa Barbara and Leiden University for helpful discussions and valuable feedback. We thank A. Upadhyaya for sharing the `BPASS+VMS` models, J. J. Eldridge and E. R. Stanway for sharing the `BPASS` models, and P. Sharda, M. R. Krumholz, A. J. Cameron, and D. Schaerer for insightful discussions. DY and JFH acknowledge support from the European Research Council (ERC) under the European Union's Horizon 2020 research and innovation program (grant agreement No. 885301). JFH acknowledges support from NSF grant No. 2307180. RAM acknowledges support from the Swiss National Science Foundation (SNSF) through project grant 200020_207349. HSBA gratefully acknowledges support from Academia Sinica through grant AS-PD-1141-M01-2. J.-T.S. and F.G. acknowledge funding by the Deutsche Forschungsgemeinschaft (DFG, German Research Foundation) - Project number 518006966 - and support by the DFG under Germany's Excellence Strategy – EXC 2121 „Quantum Universe" – 390833306. This work is based on observations made with the NASA/ESA/CSA James Webb Space Telescope, associated with program GO 9180. The data were obtained from the Mikulski Archive for Space Telescopes at the Space Telescope Science Institute, which is operated by the Association of Universities for Research in Astronomy, Inc., under NASA contract NAS 5-03127 for JWST. This paper makes use of the following ALMA data: ADS/JAO.ALMA#2023.1.00443.S ALMA is a partnership of ESO (representing its member states), NSF (USA) and NINS (Japan), together with NRC (Canada), NSTC and ASIAA (Taiwan), and KASI (Republic of Korea), in cooperation with the Republic of Chile. The Joint ALMA Observatory is operated by ESO, AUI/NRAO and NAOJ.

Claude (Anthropic) and ChatGPT (OpenAI) were used to assist with language editing and revision of the manuscript text and with the development of plotting scripts used to produce the figures. All scientific analysis, results, and conclusions are the authors' own, and the authors take full responsibility for the content of this paper.

DATA AVAILABILITY

The JWST/NIRSpec data underlying this article are available in the Mikulski Archive for Space Telescopes (MAST) under program GO 9180, and the ALMA data are available in the ALMA Science Archive under project code 2023.1.00443.S. The reduced spectra, calibrated data cubes, and other data products generated in this work will be shared on reasonable request to the corresponding author.

REFERENCES

Appenzeller I., Stahl O., Tapken C., Mehlert D., Noll S., 2005, A&A, 435, 465
Asplund M., Amarsi A. M., Grevesse N., 2021, A&A, 653, A141
Banerjee S., Kroupa P., Oh S., 2012, MNRAS, 426, 1416
Beelen A., Cox P., Benford D. J., Dowell C. D., Kovács A., Bertoldi F., Omont A., Carilli C. L., 2006, ApJ, 642, 694
Berg D. A., et al., 2025, arXiv e-prints, p. arXiv:2511.13591
Bestenlehner J. M., et al., 2014, A&A, 570, A38
Bouwens R. J., et al., 2021, AJ, 162, 47
Bouwens R. J., et al., 2022, ApJ, 931, 160
Bowler R. A. A., Dunlop J. S., McLure R. J., McLeod D. J., 2017, MNRAS, 466, 3612
Bowler R. A. A., et al., 2024, MNRAS, 527, 5808
Brinchmann J., Pettini M., Charlot S., 2008, MNRAS, 385, 769
Bunker A. J., et al., 2023, A&A, 677, A88
CASA Team et al., 2022, PASP, 134, 114501
Calzetti D., Armus L., Bohlin R. C., Kinney A. L., Koornneef J., Storchi-Bergmann T., 2000, ApJ, 533, 682
Cameron A. J., Katz H., Rey M. P., Saxena A., 2023, MNRAS, 523, 3516
Cameron A. J., et al., 2026, arXiv e-prints, p. arXiv:2601.15964
Castellano M., et al., 2022, ApJ, 938, L15
Cataldi E., et al., 2025, arXiv e-prints, p. arXiv:2512.07955
Cepa J., et al., 2000, in Iye M., Moorwood A. F., eds, Society of Photo-Optical Instrumentation Engineers (SPIE) Conference Series Vol. 4008, Optical and IR Telescope Instrumentation and Detectors. pp 623–631, doi:10.1117/12.395520
Charbonnel C., Schaerer D., Prantzos N., Ramírez-Galeano L., Fragos T., Kuruvanthodi A., Marques-Chaves R., Gieles M., 2023, A&A, 673, L7
Chen Z., Stark D. P., Endsley R., Topping M., Whitler L., Charlot S., 2023, MNRAS, 518, 5607
Chen Z., et al., 2026, arXiv e-prints, p. arXiv:2608.12699
Costa G., et al., 2025, A&A, 694, A193
Crowther P. A., 2007, ARA&A, 45, 177
Crowther P. A., Schnurr O., Hirschi R., Yusof N., Parker R. J., Goodwin S. P., Kassim H. A., 2010, MNRAS, 408, 731
Crowther P. A., et al., 2016, MNRAS, 458, 624
Cueto E. R., Hutter A., Dayal P., Gottlöber S., Heintz K. E., Mason C., Trebitsch M., Yepes G., 2024, A&A, 686, A138
De Looze I., et al., 2014, A&A, 568, A62
Decarli R., et al., 2018, ApJ, 854, 97
Dekel A., Sarkar K. C., Birnboim Y., Mandelker N., Li Z., 2023, MNRAS, 523, 3201
Dessauges-Zavadsky M., Marques-Chaves R., Schaerer D., Xiao M. Y., Colina L., Alvarez-Marquez J., Pérez-Fournon I., 2025, A&A, 693, A17
Eldridge J. J., Stanway E. R., Xiao L., McClelland L. A. S., Taylor G., Ng M., Greis S. M. L., Bray J. C., 2017, Publ. Astron. Soc. Australia, 34, e058
Erb D. K., Pettini M., Shapley A. E., Steidel C. C., Law D. R., Reddy N. A., 2010, ApJ, 719, 1168
Fan X., Bañados E., Simcoe R. A., 2023, ARA&A, 61, 373
Ferrara A., Pallottini A., Dayal P., 2023, MNRAS, 522, 3986
Ferrara A., Pallottini A., Sommovigo L., 2025, A&A, 694, A286
Figer D. F., 2005, Nature, 434, 192
Finkelstein S. L., et al., 2023, ApJ, 946, L13
Gazagnes S., Chisholm J., Schaerer D., Verhamme A., Rigby J. R., Bayliss M., 2018, A&A, 616, A29
Gräfener G., 2021, A&A, 647, A13
Gräfener G., Vink J. S., de Koter A., Langer N., 2011, A&A, 535, A56
Gürkan M. A., Freitag M., Rasio F. A., 2004, ApJ, 604, 632
Harikane Y., et al., 2022, ApJS, 259, 20
Harikane Y., et al., 2023, ApJS, 265, 5
Harikane Y., et al., 2025, ApJ, 980, 138
Horne K., 1986, PASP, 98, 609
Inami H., et al., 2022, MNRAS, 515, 3126
Inayoshi K., Visbal E., Haiman Z., 2020, ARA&A, 58, 27
Isobe Y., et al., 2023, ApJ, 959, 100
Izumi T., et al., 2021, ApJ, 908, 235

Ji X., et al., 2024, MNRAS, 535, 881
Kashikawa N., et al., 2002, PASJ, 54, 819
Killi M., et al., 2024, MNRAS, 531, 3222
Krumholz M. R., Klein R. I., McKee C. F., Offner S. S. R., Cunningham A. J., 2009, Science, 323, 754
Leitherer C., Byler N., Lee J. C., Levesque E. M., 2018, ApJ, 865, 55
Li Z., Dekel A., Sarkar K. C., Aung H., Giavalisco M., Mandelker N., Tacchella S., 2024, A&A, 690, A108
Marques-Chaves R., et al., 2020, MNRAS, 499, L105
Marques-Chaves R., Schaerer D., Álvarez-Márquez J., Colina L., Dessauges-Zavadsky M., Pérez-Fournon I., Saldana-Lopez A., Verhamme A., 2021, MNRAS, 507, 524
Marques-Chaves R., et al., 2022, MNRAS, 517, 2972
Marques-Chaves R., et al., 2024, A&A, 691, A87
Marques-Chaves R., et al., 2025, arXiv e-prints, p. arXiv:2510.12411
Marques-Chaves R., Martins F., Schaerer D., Dessauges-Zavadsky M., Palacios A., 2026, arXiv e-prints, p. arXiv:2604.21493
Martins F., Palacios A., 2022, A&A, 659, A163
Martins F., Schaerer D., Marques-Chaves R., Upadhyaya A., 2023, A&A, 678, A159
Martins F., Palacios A., Schaerer D., Marques-Chaves R., 2025, A&A, 698, A262
Mason C. A., Trenti M., Treu T., 2023, MNRAS, 521, 497
Matsuoka Y., et al., 2016, ApJ, 828, 26
Matsuoka Y., et al., 2018a, PASJ, 70, S35
Matsuoka Y., et al., 2018b, ApJS, 237, 5
Matsuoka Y., et al., 2019, ApJ, 883, 183
Matsuoka Y., et al., 2022, ApJS, 259, 18
Matsuoka Y., et al., 2023, ApJ, 949, L42
Matsuoka Y., et al., 2025, ApJS, 280, 68
Meštrić U., et al., 2023, A&A, 673, A50
Naidu R. P., et al., 2022, ApJ, 940, L14
Newville M., et al., 2025, LMFIT: Non-Linear Least-Squares Minimization and Curve-Fitting for Python, doi:10.5281/zenodo.16175987
Ocvirk P., et al., 2025, A&A, 703, A98
Ono Y., et al., 2018, PASJ, 70, S10
Pallottini A., Ferrara A., 2023, A&A, 677, L4
Portegies Zwart S. F., Makino J., McMillan S. L. W., Hut P., 1999, A&A, 348, 117
Portegies Zwart S. F., Baumgardt H., Hut P., Makino J., McMillan S. L. W., 2004, Nature, 428, 724
Prochaska J., et al., 2020, The Journal of Open Source Software, 5, 2308
Rantala A., Naab T., Lahén N., 2024, MNRAS, 531, 3770
Reddy N. A., Steidel C. C., 2009, ApJ, 692, 778
Reddy N. A., Steidel C. C., Pettini M., Bogosavljević M., Shapley A. E., 2016, ApJ, 828, 108
Roberts-Borsani G., et al., 2024, ApJ, 976, 193
Roberts-Borsani G., et al., 2025, ApJ, 983, 18
Robertson B., et al., 2024, ApJ, 970, 31
Sabhahit G. N., Vink J. S., Sander A. A. C., Higgins E. R., 2023, MNRAS, 524, 1529
Saldana-Lopez A., et al., 2022, A&A, 663, A59
Sanders R. L., et al., 2025, arXiv e-prints, p. arXiv:2508.10099
Schaerer D., Vacca W. D., 1998, ApJ, 497, 618
Schaerer D., Marques-Chaves R., Xiao M., Korber D., 2024, A&A, 687, L11
Schaerer D., Guibert J., Marques-Chaves R., Martins F., 2025, A&A, 693, A271
Schouws S., et al., 2023, ApJ, 954, 103
Senchyna P., Stark D. P., Charlot S., Chevallard J., Bruzual G., Vidal-García A., 2021, MNRAS, 503, 6112
Shapley A. E., Steidel C. C., Pettini M., Adelberger K. L., 2003, ApJ, 588, 65
Shen X., Vogelsberger M., Boylan-Kolchin M., Tacchella S., Kannan R., 2023, MNRAS, 525, 3254
Shi Y., Murray N., 2026, arXiv e-prints, p. arXiv:2603.10581
Shi Y., Grudić M. Y., Hopkins P. F., 2021, MNRAS, 505, 2753
Shi Y., Dai L., Murray N., Ye C. S., Matzner C. D., Pascale M., 2026, ApJ, 997, 309
Smith L. J., et al., 2023, ApJ, 958, 194
Stanway E. R., Eldridge J. J., 2018, MNRAS, 479, 75
Steidel C. C., Strom A. L., Pettini M., Rudie G. C., Reddy N. A., Trainor R. F., 2016, ApJ, 826, 159
Sun G., Faucher-Giguère C.-A., Hayward C. C., Shen X., Wetzel A., Feldmann R., 2023, ApJ, 955, L35
Topping M. W., et al., 2024, MNRAS, 529, 3301
Trinca A., Schneider R., Valiante R., Graziani L., Ferrotti A., Omukai K., Chon S., 2024, MNRAS, 529, 3563
Upadhyaya A., Marques-Chaves R., Schaerer D., Martins F., Pérez-Fournon I., Palacios A., Stanway E. R., 2024, A&A, 686, A185
Vanzella E., et al., 2022, A&A, 659, A2
Vink J. S., 2015, in Vink J. S., ed., Astrophysics and Space Science Library Vol. 412, Very Massive Stars in the Local Universe. p. 77 (arXiv:1406.5357), doi:10.1007/978-3-319-09596-7_4
Vink J. S., 2023, A&A, 679, L9
Vink J. S., de Koter A., Lamers H. J. G. L. M., 2001, A&A, 369, 574
Vink J. S., Muijres L. E., Anthonisse B., de Koter A., Gräfener G., Langer N., 2011, A&A, 531, A132
Vink J. S., et al., 2015, Highlights of Astronomy, 16, 51
Volonteri M., Habouzit M., Colpi M., 2021, Nature Reviews Physics, 3, 732
Welch B., et al., 2025, ApJ, 980, 33
Woosley S. E., Heger A., 2015, in Vink J. S., ed., Astrophysics and Space Science Library Vol. 412, Very Massive Stars in the Local Universe. p. 199 (arXiv:1406.5657), doi:10.1007/978-3-319-09596-7_7
Yang D., et al., 2026, A&A, 711, A104
Yusof N., et al., 2013, MNRAS, 433, 1114
Zanella A., et al., 2018, MNRAS, 481, 1976
Zhu Y., et al., 2026, ApJ, 1000, 303
Ziparo F., Ferrara A., Sommovigo L., Kohandel M., 2023, MNRAS, 520, 2445

APPENDIX A: ALMA MEASUREMENTS

We measure all ALMA quantities directly from the calibrated data cubes. For each source, we use the systemic redshift measured from the JWST/NIRSpec spectrum to predict the observed [C II] frequency, $\nu_{\rm ref} = \nu_{\rm rest}/(1 + z_{\rm NIRSpec})$. We construct the [C II] moment-0 map using $|\nu - \nu_{\rm ref}| < 0.6$ GHz, corresponding to approximately ±722 and ±738 km s^{-1} for J1450−0144 and J1429−0104, respectively. This initial window is used to identify the line-emitting region and define the extraction aperture. We subsequently fit the extracted spectrum with a free Gaussian centroid; the resulting $z_{\rm [C\,II]}$ defines the velocity zero point in Fig. 8.

Continuum maps. Continuum maps are constructed by averaging line-free channels in the ranges 262.4–267.2 GHz for J1450−0144 and 256.5–259.5 GHz for J1429−0104. The per-pixel noise $\sigma_{\rm cont}$ is estimated as the median absolute deviation (MAD-scaled) of pixels in a background annulus of 30–50 pixel radius around the source.

[C II] moment-0 maps. For each spatial pixel we subtract the continuum map from the line-window channels and integrate in velocity to produce a moment-0 map. The line-map noise $\sigma_{\rm m0}$ is computed analogously from the same background annulus.

Aperture selection. Centred on the moment-0 peak pixel, we compute an elliptical curve of growth using apertures whose semi-axes scale as $k\times$ the synthesised beam ($k = 0.5$–6.0). The fiducial aperture is the smallest one enclosing 90% of the maximum cumulative flux, yielding $2.252'' \times 1.856''$ for J1450−0144 and $1.656'' \times 1.364''$ for J1429−0104.

Spectra and [C II] fluxes. Aperture-extracted spectra are obtained by collapsing the cube with the fiducial-aperture weights, divided by the beam area in pixels. The continuum level is taken as the median of the line-free channels, and the channel noise $\sigma_{\rm chan}$ as the MAD on the same channels. We fit a single Gaussian to the continuum-subtracted spectrum within ±1.5 line-window widths and report $F_{[\mathrm{C\,II}]} = A\sigma_v\sqrt{2\pi}$, with the uncertainty propagated from the fitted A and σ_v. We additionally extract a peak-pixel spectrum at the moment-0 peak and fit it identically. J1450−0144 is consistent with an unresolved point source, so we adopt the peak-pixel flux as our fiducial value; J1429−0104 is resolved and we adopt the aperture flux. The two spectra are shown in Fig. 8.

Continuum flux densities. The aperture continuum flux is $S_\nu = \sum_{i\in\mathrm{ap}} w_i\, C_i/\Omega_{\mathrm{beam}}$, where C_i is the continuum map, w_i are the exact-pixel aperture weights, and Ω_{beam} is the beam area in pixels. Its uncertainty is $\sigma_{\mathrm{cont}}\sqrt{N_{\mathrm{beams}}}$, with N_{beams} the number of beams subtended by the aperture.

APPENDIX B: CONTINUUM FITTING

Fig. B1 shows the spline continuum models of both sources, constructed as described in Sect. 2.2.2, together with the per-pixel residuals and their distributions. These fits define the continuum used for all line and equivalent-width measurements in this work.

This paper has been typeset from a TEX/LATEX file prepared by the author.

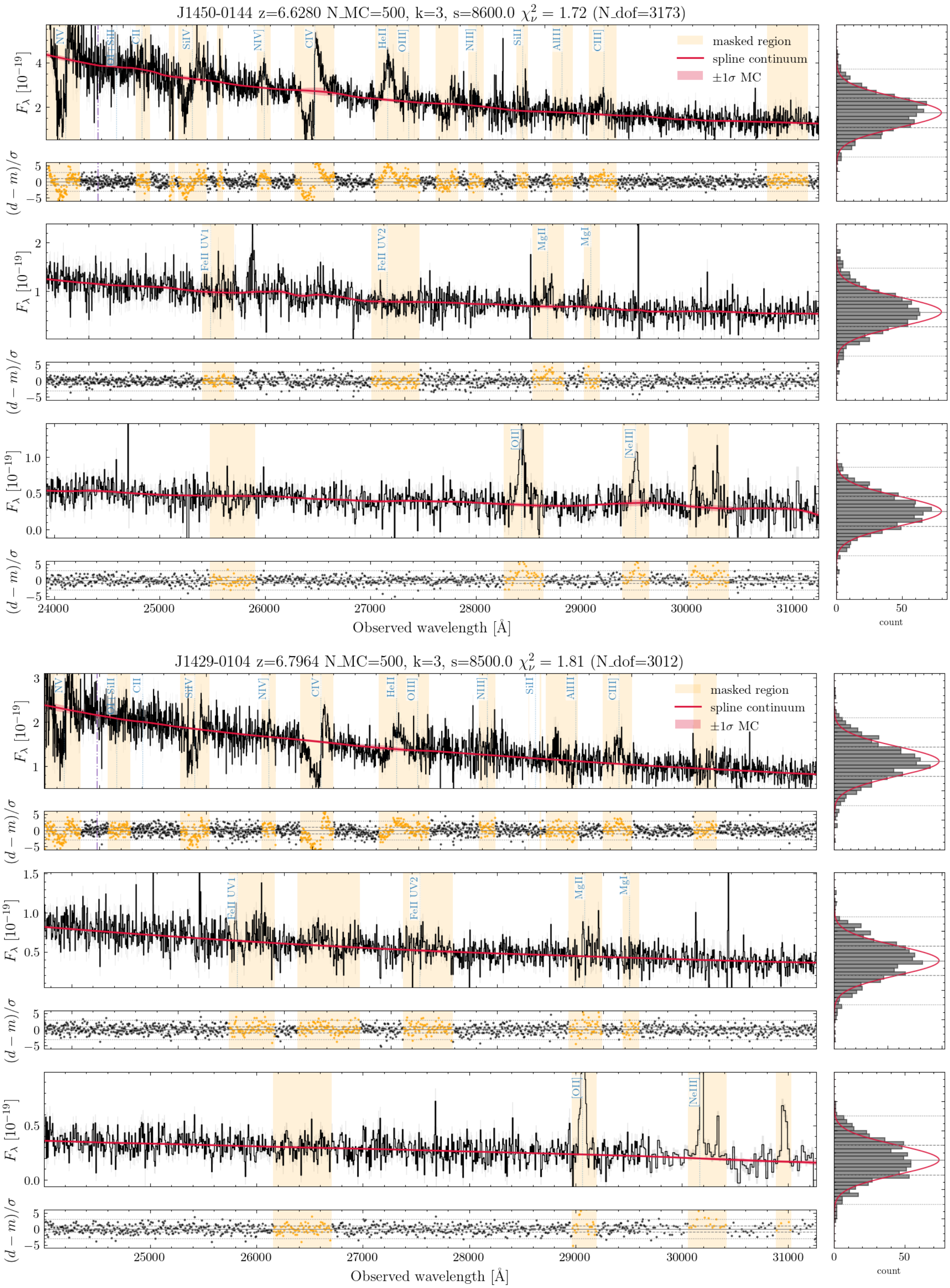

Figure B1. Spline continuum fits of J1450−0144 (top) and J1429−0104 (bottom). See Sect. 2.2.2 for details. Each pair of panels shows the observed spectrum (black) with the median continuum model (red, $\pm 1\sigma$ shaded) and the per-pixel residuals $(d-m)/\sigma$ below. Right-hand panels show the residual distributions. Shaded bands mark wavelength windows excluded from the fit.